Climate
of the Past

A transient coupled general circulation model (CGCM) simulation of the past 3 million years

Kyung-Sook Yun[1,2], Axel Timmermann[1,2,⚲], Sun-Seon Lee[1,2], Matteo Willeit[3], Andrey Ganopolski[3], and Jyoti Jadhav[1,2]

[1]Center for Climate Physics, Institute for Basic Science (IBS), Busan, Republic of Korea
[2]Pusan National University, Busan, Republic of Korea
[3]Potsdam Institute for Climate Impact Research, Potsdam, Germany
⚲*Invited contribution by Axel Timmermann, recipient of the EGU Milutin Milankovic Medal 2015.*

Correspondence: Kyung-Sook Yun (kssh@pusan.ac.kr) and Axel Timmermann (axel@ibsclimate.org)

Abstract. Driven primarily by variations in the earth's axis wobble, tilt, and orbit eccentricity, our planet experienced massive glacial/interglacial reorganizations of climate and atmospheric CO_2 concentrations during the Pleistocene (2.58 million years ago (Ma)–11.7 thousand years ago (ka)). Even after decades of research, the underlying climate response mechanisms to these astronomical forcings have not been fully understood. To further quantify the sensitivity of the earth system to orbital-scale forcings, we conducted an unprecedented quasi-continuous coupled general climate model simulation with the Community Earth System Model version 1.2 (CESM1.2, $\sim 3.75°$ horizontal resolution), which covers the climatic history of the past 3 million years (3 Myr). In addition to the astronomical insolation changes, CESM1.2 is forced by estimates of CO_2 and ice-sheet topography which were obtained from a simulation previously conducted with the CLIMBER-2 earth system model of intermediate complexity. Our 3 Ma simulation consists of 42 transient interglacial/glacial simulation chunks, which were partly run in parallel to save computing time. The chunks were subsequently merged, accounting for spin-up and overlap effects to yield a quasi-continuous trajectory. The computer model data were compared against a plethora of paleo-proxy data and large-scale climate reconstructions. For the period from the Mid-Pleistocene Transition (MPT, ~ 1 Ma) to the late Pleistocene we find good agreement between simulated and reconstructed temperatures in terms of phase and amplitude (-5.7 °C temperature difference between Last Glacial Maximum and Holocene). For the earlier part (3–1 Ma), differences in orbital-scale variability occur between model simulation and the reconstructions, indicating potential biases in the applied CO_2 forcing. Our model-proxy data comparison also extends to the westerlies, which show unexpectedly large variance on precessional timescales, and hydroclimate variables in major monsoon regions. Eccentricity-modulated precessional variability is also responsible for the simulated changes in the amplitude and flavors of the El Niño–Southern Oscillation. We further identify two major modes of planetary energy transport, which played a crucial role in Pleistocene climate variability: the first obliquity and CO_2-driven mode is linked to changes in the Equator-to-pole temperature gradient; the second mode regulates the interhemispheric heat imbalance in unison with the eccentricity-modulated precession cycle. During the MPT, a pronounced qualitative shift occurs in the second mode of planetary energy transport: the post-MPT eccentricity-paced variability synchronizes with the CO_2 forced signal. This synchronized feature is coherent with changes in global atmospheric and ocean circulations, which might contribute to an intensification of glacial cycle feedbacks and amplitudes. Comparison of this paleo-simulation with greenhouse warming simulations reveals that for an RCP8.5 greenhouse gas emission scenario, the projected global mean surface temperature changes over the next 7 decades would be comparable to the late Pleistocene glacial-interglacial range; but the anthropogenic warming rate will exceed any previous ones by a factor of ~ 100.

1 Introduction

Glacial cycles during the Pleistocene (2.58 million years ago (Ma) to 11.7 thousand years ago (ka)) were characterized by global mean surface temperature (GMST) swings that attained values of up to $\sim 6\,°C$ (Schneider Von Deimling et al., 2006; McClymont et al., 2013; Tierney et al., 2020). These variations in temperature and the associated waxing and waning of continental ice sheets were accompanied by relatively small changes ($< \sim 0.5\,W\,m^{-2}$) in the earth's global mean radiation balance (Baggenstos et al., 2019), but considerable variations in the seasonal and latitudinal distribution of insolation (Masson-Delmotte et al., 2013). Transient coupled atmosphere/ocean simulations either with earth system models of intermediate complexity (EMICs) (Menviel et al., 2011; Timm and Timmermann, 2007; Timm et al., 2008; Timmermann et al., 2009, 2014b; Timmermann and Friedrich, 2016) or based on coupled general circulation models (CGCMs) (Timmermann et al., 2007, 2022; Liu et al., 2009; Singarayer and Valdes, 2010; Zhang et al., 2021) have helped elucidate how orbital-scale forcings translate into global and regional climate responses. Transient orbital-scale ice-sheet sensitivities and feedbacks with the atmosphere and ocean have so far only been explored with intermediate-complexity models (Ganopolski et al., 2010; Willeit and Ganopolski, 2018; Willeit et al., 2019; Heinemann et al., 2014) or forced offline ice-sheet models with various representations of climatic feedbacks (Tigchelaar et al., 2018, 2019; Abe-Ouchi et al., 2013).

To gain a better understanding of how glacial/interglacial variability emerged during the Pleistocene, it has been beneficial to study the lateral flow of energy in our climate system. Orbital-scale shifts in atmospheric and oceanic heat transports influence key atmospheric circulation features such as the Hadley circulation, the Intertropical Convergence Zones (ITCZs), and mid-latitude storm tracks (Liu et al., 2015, 2017; Chiang and Bitz, 2005; Kaspar et al., 2007). Previous modeling studies (Timmermann et al., 2014b; Liu et al., 2017; Kamae et al., 2016; Donohoe et al., 2020; Kim, 2004) have elucidated the relationship between external forcings, climate feedbacks, and lateral energy redistributions by focusing on specific Pleistocene periods, such as the Last Glacial Maximum (LGM) or extreme orbital conditions. However, little is known on how the interplay between orbital and greenhouse gas forcing (GHG) has shaped the meridional transport of heat in the atmosphere and ocean over the past 3 million years (Myr) and whether these two components reinforced or compensated each other (Bjerknes, 1964; Stone, 1978). To understand how Milanković forcing generates glacial variability, it is necessary to determine how changes in atmospheric and oceanic heat transports feed back to the climate mean state. This is particularly interesting in the context of the Mid-Pleistocene Transition (MPT; ~ 1.25–0.7 Ma) when the dominant periodicity of ice volume and global mean temperature changed from 41 to 80–

120 thousand year (kyr) cycles (Clark et al., 2006; Bintanja and van de Wal, 2008; McClymont et al., 2013).

To address these fundamental questions, we conducted an unprecedented transient CGCM simulation that covers the climate history of the past 3 Myr. This quasi-continuous model simulation, represents a 1 Myr extension of the 2 Ma Community Earth System Model (CESM) simulation, which has originally been conducted to study how climate shaped early human habitats (Timmermann et al., 2022). The 2 and 3 Ma simulations are based on the CESM version 1.2 in 3.75° atmospheric and nominal 3° oceanic horizontal resolutions (T31_gx3v5). Our CESM1.2 3 Ma simulation represents the first full Pleistocene transient model simulation conducted with a 3 dimensional CGCM to date and it has been used previously (Zeller et al., 2023; Ruan et al., 2023; Margari et al., 2023) to determine and quantify the effects of past climate shifts on different human evolutionary processes.

This paper describes the overall performance of the 3 Ma climate simulation and highlights important processes related to changes in Pleistocene global heat transport, feedbacks, and variability. The paper is organized as follows. Section 2 introduces the model set-up and experimental design and discusses several disadvantages of the modeling approach. In Sect. 3, we compare the simulation with proxy data for mean temperature, hydroclimate, and large-scale westerly winds. Section 4 illustrates how the large-scale external forcings can influence modes of natural climate variability, exemplified here by the El Niño–Southern Oscillation (ENSO) phenomenon. We then investigate the global energy transport changes in Sect. 5 and the related large-scale atmosphere and ocean changes in Sect. 6. Section 7 discusses the main results and provides a future outlook.

2 Model set-up and experimental design

Our transient Pleistocene paleoclimate model simulation uses the coupled CESM version 1.2 (Hurrell et al., 2013), with CAM4 atmospheric physics (T31, $\sim 3.75°$ resolution, 26 levels), the POP2 ocean model (gx3v5, 100×116 horizonal grids and 25 vertical levels), CLM4.0 land physics (prescribed vegetation), and CICE4 (Los Alamos Sea Ice Model) sea ice components. Unlike previous transient EMIC simulations (Willeit et al., 2019; Timmermann et al., 2014b; Ganopolski et al., 2010; Goosse et al., 2010), the CESM1.2 simulation includes more realism and complexity, e.g., interactive clouds, a realistic representation of tropical processes, a 3-dimensional ocean circulation, and a fully dynamic atmosphere. We split the simulation into 42 chunks (minimum chunk length 32 kyr and maximum length 125 kyr) which overlapped by about 5000 years (see Fig. 1a) and ran them in parallel on the ICCP/IBS supercomputer *Aleph*. Each chunk was initialized with peak interglacial conditions (maximum boreal summer insolation, e.g., 125, 243 ka, and so on) using the same initial and restart data from a preindustrial

Figure 1. "3 Ma" ensemble simulation strategy. **(a)** Transient climate variability of summer insolation at 65° N, CO_2, and ice volume in sea level equivalent (SLE, m) from Willeit et al. (2019). Each color shading indicates the respective period of 42 individual ensemble simulations. **(b, c)** Scatter plot of **(b)** summer insolation versus CO_2, and **(c)** SLE versus CO_2. Each ensemble run was initiated at interglacial peaks (e.g., 125 and 243 ka) of having higher CO_2 and lower ice volume, as displayed by colored dots.

2300-year-long spin-up control simulation and then orbital forcings (Berger, 1978), and estimates of greenhouse gases and ice-sheet albedo and topography (Willeit et al., 2019) were applied. In our simulation, we did not account for the freshwater forcing originating from the ice sheets, which will likely lead to an underestimation of the simulated Atlantic Meridional Overturning Circulation (AMOC) variability, both on orbital (Timmermann et al., 2010) and millennial (Menviel et al., 2014) timescales. We finally obtained the "3 Ma" full history of climate by concatenating the data from each chunk a posteriori and by applying a time-sliding linear interpolation for the overlap periods following the methodology of an earlier study (Timmermann et al., 2014b).

We also applied the acceleration technique (Lorenz and Lohmann, 2004; Lunt et al., 2006) to the external forcings (i.e., orbital, GHG, and ice-sheets forcings) of the 3 Ma

transient simulation. Using this method with an acceleration factor of 5 reduces the 3 000 000 orbital year forcing to 600 000 model years in CESM. Previous studies have demonstrated that accelerated simulations with acceleration factors of less than 10 reproduce well the unaccelerated climate response to external forcings, except for deep ocean variables and some surface ocean variables in high-latitude regions where the climate is closely connected to the deep ocean (Timm and Timmermann, 2007; Varma et al., 2016; Lunt et al., 2006). Our choice of a relatively small acceleration factor of 5 (Timmermann et al., 2014b) presents a reasonable compromise between increasing computational performance and minimizing disequilibrium processes. Moreover, with an acceleration factor of 5 the fastest "accelerated" forcing timescale (Timm and Timmermann, 2007) – i.e., the precessional cycle – is applied as a ~ 4000 year model forc-

ing, which allows the deep ocean to adjust at least on advective timescales (Friedrich and Timmermann, 2012). However, for deep-ocean diffusive processes, we would still expect disequilibrium effects for the precessional cycle, but less distortion for obliquity and eccentricity scales.

The CESM uses the constant LGM ocean bathymetry and land-sea mask (i.e., 21 ka) based on ICE-6G_C data (Argus et al., 2014). This choice can in principle generate large-scale climate biases due to glacial/interglacial changes in land-sea distributions, in areas such as the Sunda and Sahul shelves (Di Nezio et al., 2016), the Bering Strait (Hu et al., 2012), and the Falkland Islands (Malvinas) continental shelf. However, the alternative of running a volume-conserving Boussinesq ocean model (POP2) with time-evolving sea level and ocean volume may also cause ambiguities and biases that have not been fully explored yet.

Figure 1a illustrates the temporal evolution of CESM1.2 forcings: orbital forcing (represented here by summer insolation at 65° N), greenhouse gas forcing (represented by the time-varying CO_2 in CESM1.2), and topographic and albedo forcing due to ice-sheet changes (represented here by the global ice volume in sea level equivalent) (Willeit et al., 2019). Overall, the interglacial peaks (initial time at each ensemble simulation, colored dots in Fig. 1b and c) are characterized by high CO_2 concentrations and low ice volume, with the orbital phase being less constrained (Fig. 1b and c). In our 3 Ma experiment, we updated the forcings of GHG concentrations (Lüthi et al., 2008; Willeit et al., 2019; Lisiecki and Raymo, 2005), Northern Hemisphere (NH) ice-sheet extent and topography (Willeit et al., 2019), and astronomical insolation variations (Berger, 1978) every 100 orbital years (i.e., 20 model years). For GHGs, we combined different datasets: after 800 ka, measured air-bubble CO_2 concentrations from the European Project for Ice Coring in Antarctica (EPICA) Dome C ice core (Jouzel et al., 2007) were used; prior to 800 ka, we used the simulated CO_2 from the CLIMBER-2 transient simulation (Willeit et al., 2019), which includes an interactive carbon cycle. We also included estimates of the CH_4 and N_2O concentrations as a CESM forcing using a regression of the EPICA CH_4 and N_2O concentrations with the global benthic $\delta^{18}O$ stack (Lisiecki and Raymo, 2005) (post 800 ka) and extended this linear statistical model to 3 Ma using the benthic $\delta^{18}O$ stack data (see Fig. S1). The ice mask and ice-sheet topography changes were also obtained from the simulated CLIMBER-2 orography data. It is worth mentioning that before the past 1 Myr, our applied orbital forcing (Berger, 1978) is somewhat different from that of later numerical estimates (Laskar et al., 2004). This discrepancy in pre-MPT orbital forcing and the resulting changes in the climate system need to be evaluated in future work. CESM1.2 in our resolution has a relatively weak equilibrium climate sensitivity of 2.4 °C warming for a doubling relative to preindustrial CO_2 levels. This is about 1.5-fold smaller than the Coupled Model Intercomparison Project Phase 6 (CMIP6) multi-model ensemble-based estimation (3.7 ± 1.1 °C within

37 multi-models) (Meehl et al., 2020). To compensate for this relatively weak climate sensitivity of CESM1.2 and to indirectly account for the effect of unresolved and highly uncertain dust forcing (Friedrich et al., 2016; Kohler et al., 2010), which is also correlated with the reconstructed CO_2 or the benthic $\delta^{18}O$ stack, we re-scaled the GHGs forcing anomalies relative to preindustrial conditions by a factor of 1.5.

3 Model-proxy comparison

3.1 Climate sensitivity and polar amplification

An important question to address is whether the 3 Ma simulation reproduces the magnitude and timing of glacial/interglacial variability during the Pleistocene. We first compare results of our 3 Ma simulations with a variety of long-term paleo-proxy data and the CLIMBER-2 simulation. Figure 2a illustrates the model's capability in capturing the magnitude and timing of GMST variations, shown by previous model- and proxy-based estimates (Willeit et al., 2019; Friedrich et al., 2016). Our simulation exhibits a −5.7 °C glacial cooling for LGM (∼ 21 ka) relative to preindustrial conditions (∼ 0 ka). This magnitude of cooling agrees well with a combined proxy-model estimate of −6.3 to −5.6 (95 % confidence interval) (e.g., Tierney et al., 2020). Simulated sea surface temperatures (SSTs) also reveal a high degree of coherence for the post-MPT period with tropical proxy-based SST reconstructions (Herbert et al., 2010) (Fig. 2b) and elsewhere (Petrick et al., 2019; Cartagena-Sierra et al., 2021; Lawrence et al., 2009; de Garidel-Thoron et al., 2005; Russon et al., 2010) (Fig. 2c–g), indicating a reliable simulation of spatial SST patterns in addition to the temporal evolution. However, prior to the MPT, the model simulation diverges considerably from some of the SST proxies in terms of representing the exact orbital phase, as well as the long-term extratropical gradual Pleistocene trends. For instance, the tropical SST stack (Herbert et al., 2010) exhibits higher pre-MPT variability on obliquity timescales of 41 kyr (Fig. 3a), as compared to the 3 Ma simulation, which features a more pronounced precessional cycle (∼ 21 kyr) (Fig. 3b). This mismatch might be in part due to an unrealistic orbital-scale variability (e.g., presence of precession) of the estimated pre-MPT CO_2 forcing (Fig. 3c) or potential seasonal biases of some of the SST alkenone proxies in the tropics (Timmermann et al., 2014a).

Various temperature reconstructions and simulations reveal amplified Arctic/Antarctic surface air temperature changes on glacial/interglacial timescales relative to the global average (Stap et al., 2018). This polar amplification is very pronounced in temperature reconstructions based on the EPICA Dome C ice core (Jouzel et al., 2007) and North Greenland Ice Core Project (NGRIP) (Barker et al., 2011), with Greenland's amplification being about twice as strong as Antarctica's, as documented by the LGM cooling of −18.2 °C for Greenland and −9.5 °C for Antarctica (Fig. 4a and b). Stronger polar amplification in Green-
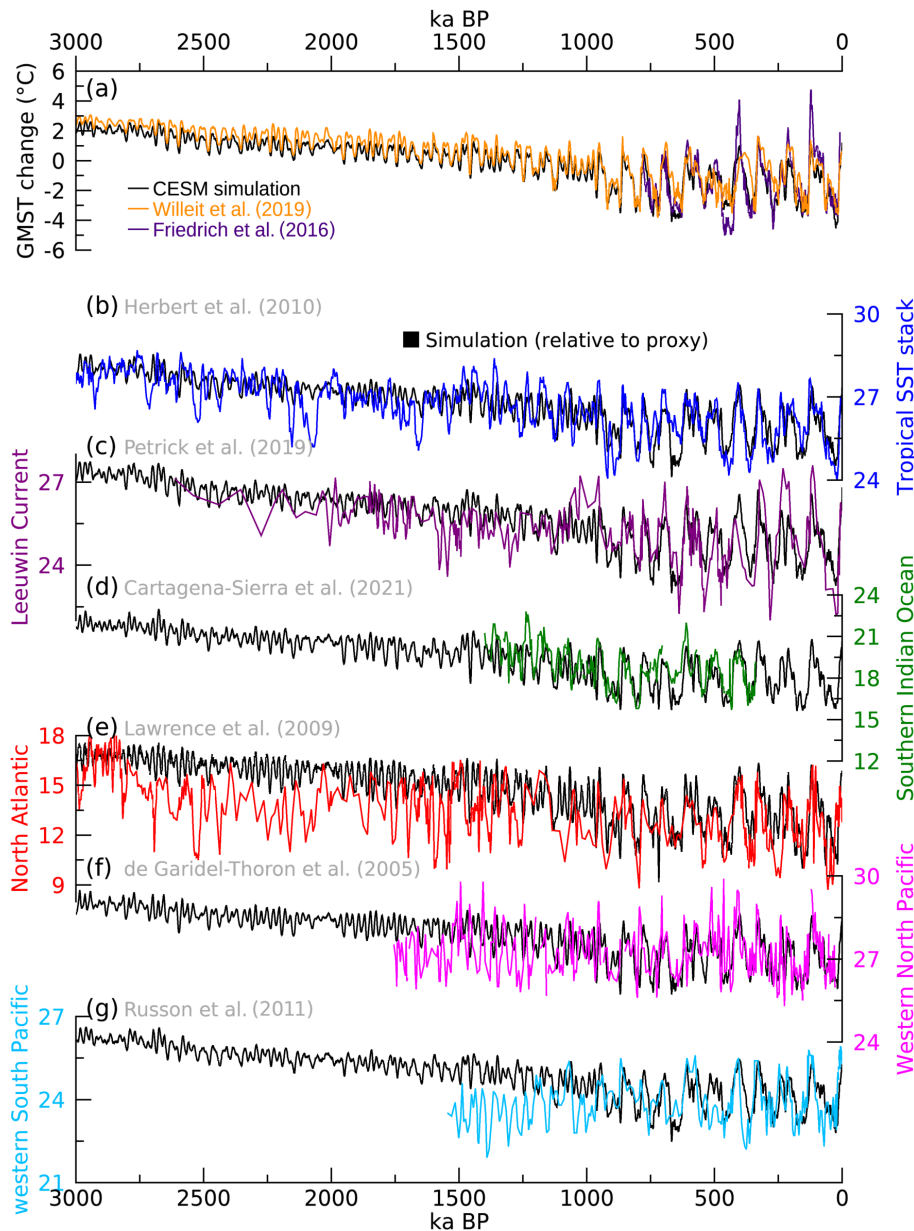
Figure 2. CESM 3 Ma simulation and climate sensitivity. **(a)** The simulated global averaged annual mean surface air temperature anomalies relative to the mean over the entire 3 Ma (black). Previous global mean temperature estimates are displayed in different colors: orange (Willeit et al., 2019) and violet (Friedrich et al., 2016). **(b–g)** Annual mean SST comparison between paleo-proxy data and CESM simulation (black): **(b)** tropical SST stack (Herbert et al., 2010) and tropical SST simulation (averaged over 5° S–5° N, unit: °C), **(c)** Leeuwin Current from Integrated Ocean Drilling Program (IODP) site U1460 (Petrick et al., 2019). **(d)** Southern Indian Ocean from sediment core MD96-2048 (Cartagena-Sierra et al., 2021). **(e)** North Atlantic from Ocean Drilling Program (ODP) 982 (Lawrence et al., 2009), **(f)** Western North Pacific from International Marine Global Change Study (IMAGES) core MD97-2140 (de Garidel-Thoron et al., 2005), and **(g)** western South Pacific from MD06-3018 (Russon et al., 2010). The proxy locations are also displayed in Fig. S2.

land can be partly explained by a larger lapse rate feedback (Hahn et al., 2020) and local impacts from the extensive NH ice sheets (Smith and Gregory, 2012). The 3 Ma simulation also captures the difference in polar amplification between Greenland and Antarctica: the amplitude of LGM cooling attains values of $\sim -15.7\,°C$ for Greenland (75° N, 42° W) and

$-8.6\,°C$ for Antarctica (75° S, 123° E). The simulation also captures well the higher post-MPT variability on eccentricity timescales of 100 kyr (Fig. 4c and d) and the rapid trends of deglacial warming in both the NH and Southern hemisphere (SH), which can be explained by a similar evolution of the GHG (Fig. 1a). Overall, temperature reconstructions
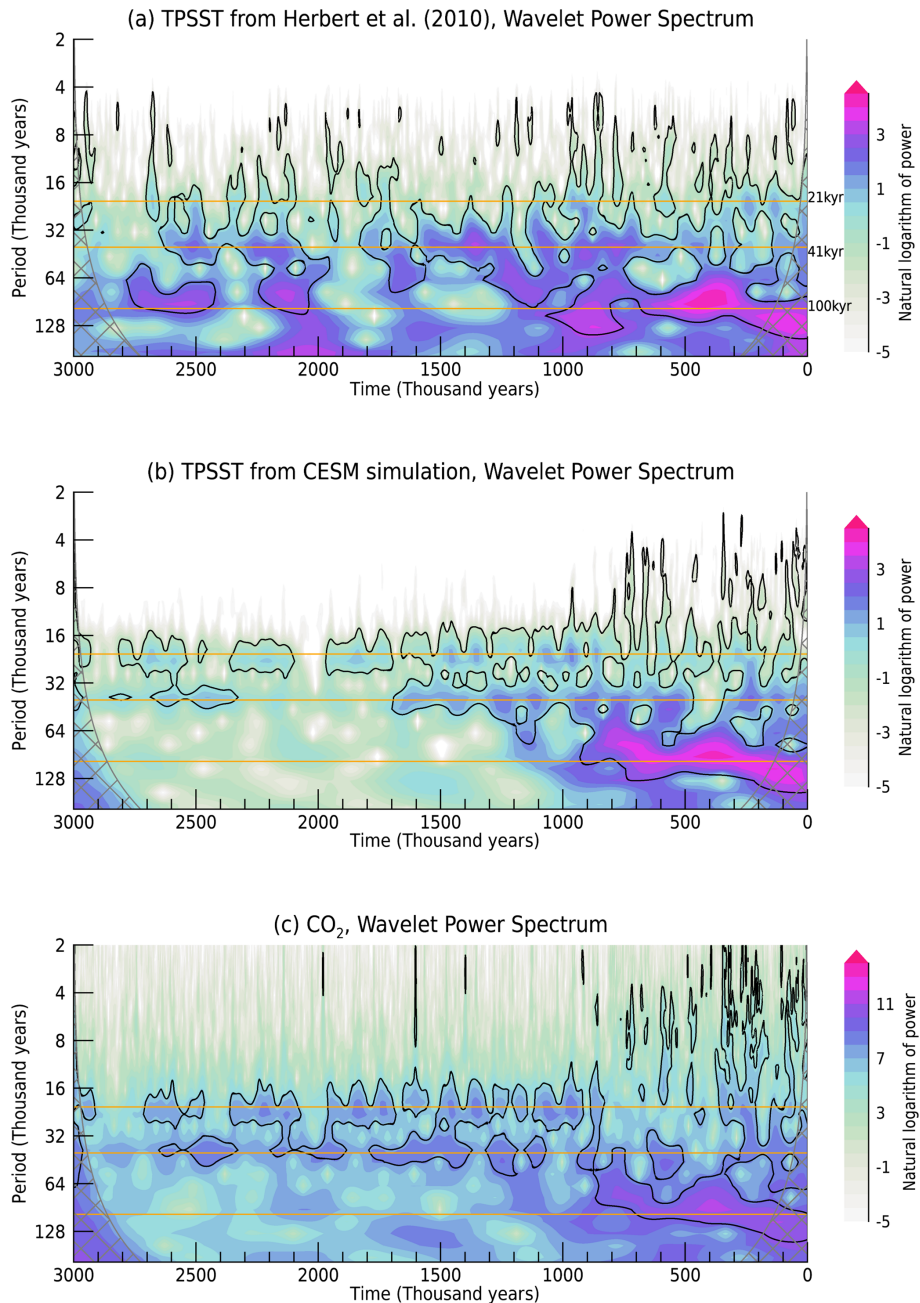
Figure 3. Wavelet power spectrum of tropical SSTs and CO_2. The wavelet power spectrum of **(a, b)** tropical SST obtained from **(a)** alkenone data and **(b)** CESM simulation and of **(c)** CO_2 concentration. The black contour indicates the value significant at the 95 % confidence level. The horizonal orange lines show 21 kyr (precession), 41 kyr (obliquity), and 100 kyr (eccentricity) periods.

from Greenland and Antarctica (Jouzel et al., 2007; Barker et al., 2011; Kindler et al., 2014) correlate well on orbital timescales with the 3 Ma simulation. These results reflect the high fidelity of the climate sensitivity of the simulation on global and regional scales and its response to the variety of acting forcings. Our simulation also provides a model-based glimpse into what temperature variability to expect in on-going ice-core projects (Lilien et al., 2021) that plan to re-

trieve Antarctic ice, which is significantly older than the old-est EPICA ice.

3.2 Hydroclimate and large-scale westerly variability

Apart from the mean temperatures, orbital-scale changes in large-scale temperature gradients also play a crucial role in driving anomalies in hydroclimate (Schneider et al., 2014) and the extratropical atmospheric circulation (Timmermann
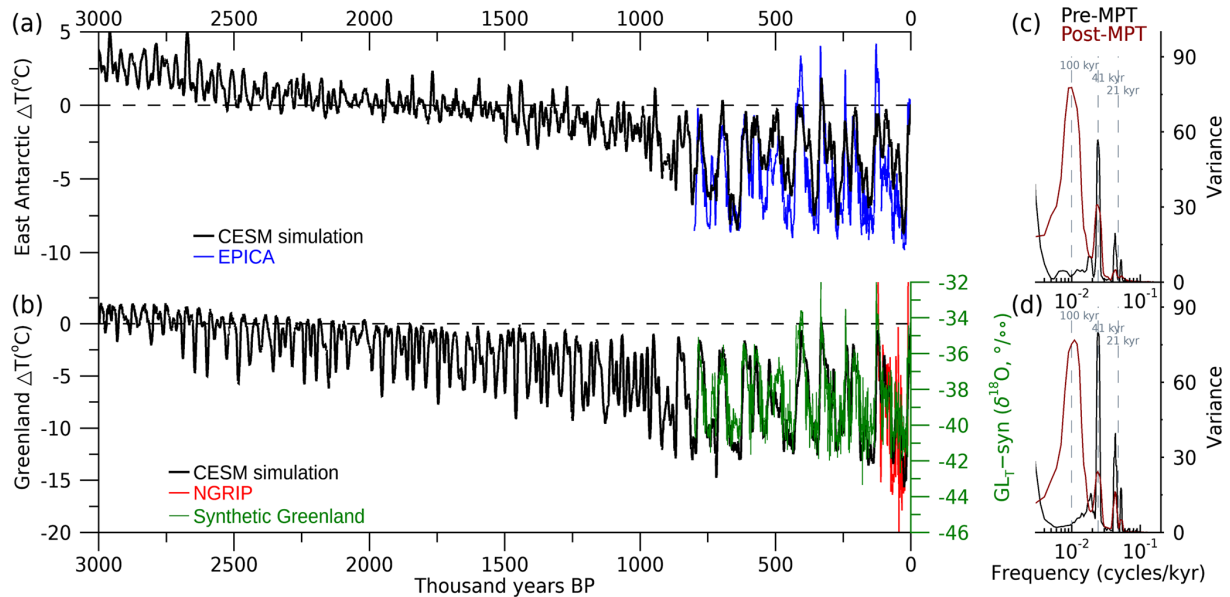
Figure 4. Polar climate changes. **(a, b)** The simulated annual mean surface air temperature anomalies relative to 0 ka in east Antarctica (**a**; 75° S, 123° E) and in Greenland (**b**; 75° N, 42° W) (black lines). Proxy-based estimations, i.e., Antarctic temperature from European Project for Ice Coring in Antarctica (EPICA) Dome C ice core (Jouzel et al., 2007; blue in upper part), North Greenland Ice Core Project (NGRIP) Greenland temperature (Kindler et al., 2014; red in bottom part; left axis), Synthetic reconstruction of Greenland δ^{18}O (Barker et al., 2011; green in bottom; right axis), scaled to match the δ^{18}O/temperature range in Kindler et al. (2014), are also displayed. **(c, d)** Spectral variance of simulated pre-MPT (3Ma-2Ma; black) and post-MPT (1–0 Ma; brown) temperatures in east Antarctica **(c)** and Greenland **(d)**. The vertical dashed lines show 21 kyr (precession), 41 kyr (obliquity), and 100 kyr (eccentricity) periods.

et al., 2014b). Here we compare simulated changes in precipitation and atmospheric westerlies with proxy-data that show strong sensitivity to these factors.

As the rising branch of the Hadley circulation, the ITCZ is characterized by a belt of deep convective precipitation near the Equator. Paleoclimate studies suggest that the latitudinal migration of the ITCZ was mainly driven by the precessional cycle (Schneider et al., 2014; Clement et al., 2004; Davis and Brewer, 2009; Liu et al., 2015). For low precession values (i.e., NH summer perihelion), NH summers receive more insolation, which leads to summer warming and a northward migration of the ITCZ and Hadley circulation (e.g., Kang et al., 2018; Tigchelaar and Timmermann, 2016). Our simulation reaffirms the precession-driven ITCZ movement (Fig. 5f and g), which is further amplitude-modulated by the 100 and 405 kyr eccentricity cycles, in agreement with some proxy records from tropical South America and Africa (Fig. 5c). Our simulation emphasizes the importance of the 405 kyr eccentricity cycle in tropical hydroclimate, which has received less attention in previous studies. Since precipitation is a positive definite non-Gaussian climate variable, the 100 and 405 kyr amplitude modulations of the precessional cycle (Fig. 5b) also rectify into a long-term mean signal (as illustrated here for Cariaco Basin precipitation; orange line in Fig. 5c) with the same frequencies, thereby introducing eccentricity as a mean forcing into the climate system (Fig. 5g).

The seasonal migration of the Hadley cell is also linked to shifts in the global monsoon precipitation (An et al., 2015; Schneider et al., 2014). With the precessional cycle modulating the amplitude of the seasonal solar forcing, monsoon systems, such as the Indian, East Asian, African, and Australia monsoons, thus show dominant variability on precessional timescales (Fig. 6) as well as contributions on obliquity and eccentricity timescales (Fig. 6e–h). Previous studies demonstrated that the past global monsoon precipitation variabilities were controlled by the orbitally driven land–sea thermal contrast, meridional pressure gradients, atmospheric CO_2 concentrations, and the growth of the NH ice sheet (Clemens and Prell, 2003; Clark et al., 2006; Kutzbach and Guetter, 1986). Although the global monsoons share similar dynamics and behaviors, there are distinct features of regional monsoon systems that need to be considered. For example, the proxy-inferred western Australia monsoon precipitation was weakened, and the amplitude of variability was strengthened during the late Pleistocene (Fig. 6a). The amplitude of observed Indian summer monsoon variability increased after 1.5 Ma to mid-Pleistocene and then decreased during the late Pleistocene (Fig. 6b). Whereas the reconstructed East Asian summer monsoon proxy shows a gradual increase in variability from 1.5 Ma to mid-late Pleistocene (An et al., 2015) (Fig. 6c), this trend in variability is absent in the reconstructed African monsoon (Fig. 6d) proxy (see Fig. S3). The situation is relatively well produced for the
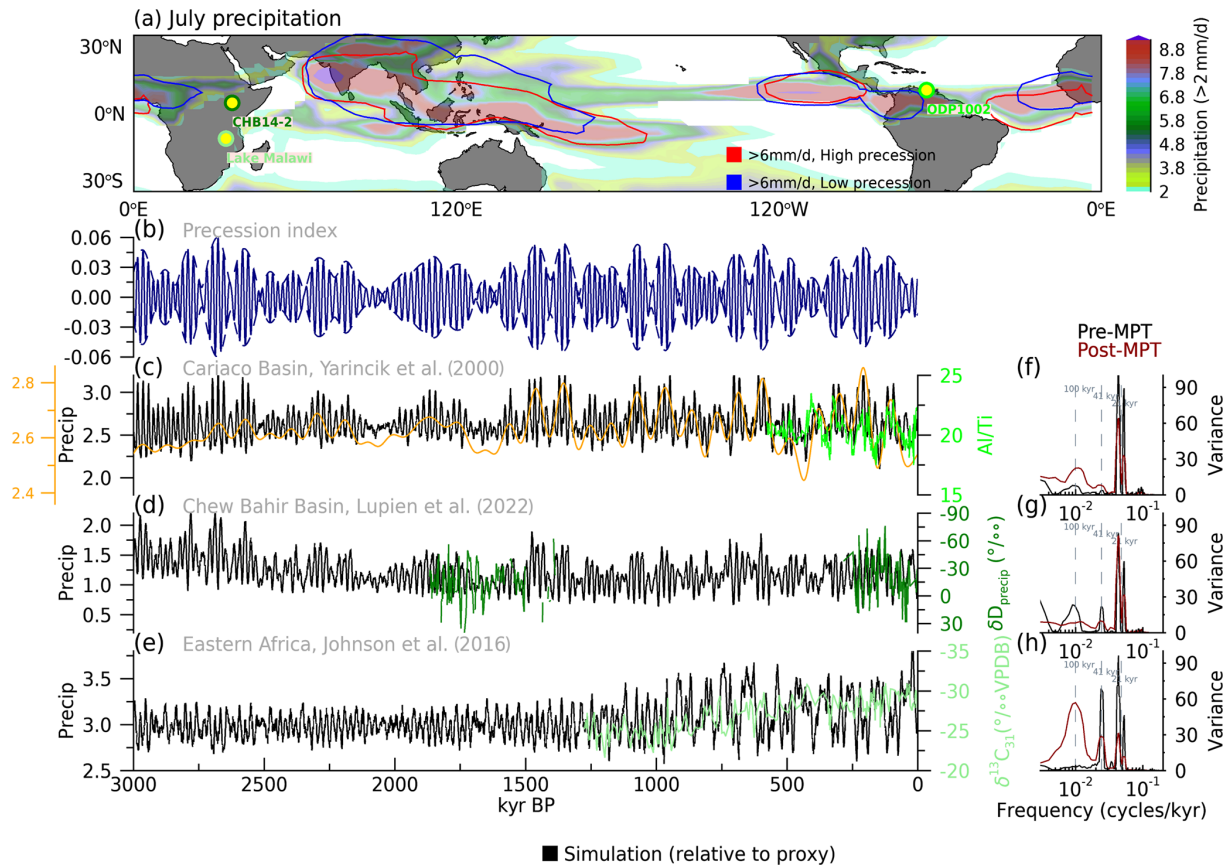
Figure 5. ITCZ changes. **(a)** Simulated July precipitation pattern (unit: mm d^{-1}) averaged for the 3 Myr period. Each proxy location is displayed in different colors. The tropical precipitation regions greater than 6 mm yr^{-1} are displayed for comparison between the phases with high precession (red) and low precession (blue). **(b)** Precession index ($e \cdot \sin\overline{\omega}$ where e is the eccentricity and $\overline{\omega}$ is the moving longitude of the perihelion). **(c–e)** Precipitation comparison between the proxy and simulation (black): **(c)** Cariaco Basin from ODP 1002 Al/Ti ratio (Yarincik et al., 2000), **(d)** Chew Bahir Basin and Turkana Basin from CHB14-2 and WTKB δD_{precip} (Lupien et al., 2022), and **(e)** Eastern Africa from Lake Malawi $\delta^{13}C_{31}$ (Johnson et al., 2016). The orange line in **(c)** indicates the 80 kyr low-pass filtered Cariaco Basin precipitation in simulation. **(f–h)** Spectral variance of simulated pre-MPT (3–2 Ma; black) and post-MPT (1–0 Ma; brown) precipitations in Cariaco Basin **(f)**, Chew Bahir Basin **(g)**, and Eastern Africa **(h)**. The vertical dashed lines show 21 kyr (precession), 41 kyr (obliquity), and 100 kyr (eccentricity) periods.

3 Ma simulation, where we see an intensification in variability for all monsoon systems, except for Africa. The 100 kyr cyclicity in all monsoon systems, except for Eastern Asia, which is dominated more by obliquity variability in proxies (Clemens et al., 2018) and simulation (Fig. 6c and g), becomes stronger after the MPT (Fig. 6e–h). This intensification in the model is likely brought about by the intensifying amplitudes of ice-sheet and CO_2 forcings and the corresponding impacts on NH hydroclimate.

We next compare the simulated large-scale westerly wind changes with dust and marine productivity reconstructions from ice cores and marine sediment proxies. Figure 7 displays the simulated westerly wind changes in the Pacific and Atlantic Ocean of both the NH and SH. We can see clear precessional and obliquity-scale variability in the simulation, consistent with some wind-sensitive climate and biogeo-

chemical proxies (Lamy et al., 2019; Naafs et al., 2012). For example, the regional characteristics such as strong obliquity response in the North Atlantic (Fig. 7b and f) and a precession signal in the South Pacific (Fig. 7d and h) are captured qualitatively in the model. In our model simulation, there is a pronounced strengthening in the variability of the westerly jet stream after the MPT, which is attributable to the larger glacial cycle amplitudes (Fig. 2a) and CO_2-induced polar amplification (Fig. 4) and resultant stronger differences in the meridional temperature gradient. The 100 kyr cyclicity in the westerlies was also strengthened considerably after the MPT, except for the North Pacific (Fig. 7f–i). Overall, the agreement between model-simulated variability and the proxy record further supports the fidelity of our modeling approach. A more in-depth regional comparison between climate model and proxies, which would account for proxy un-
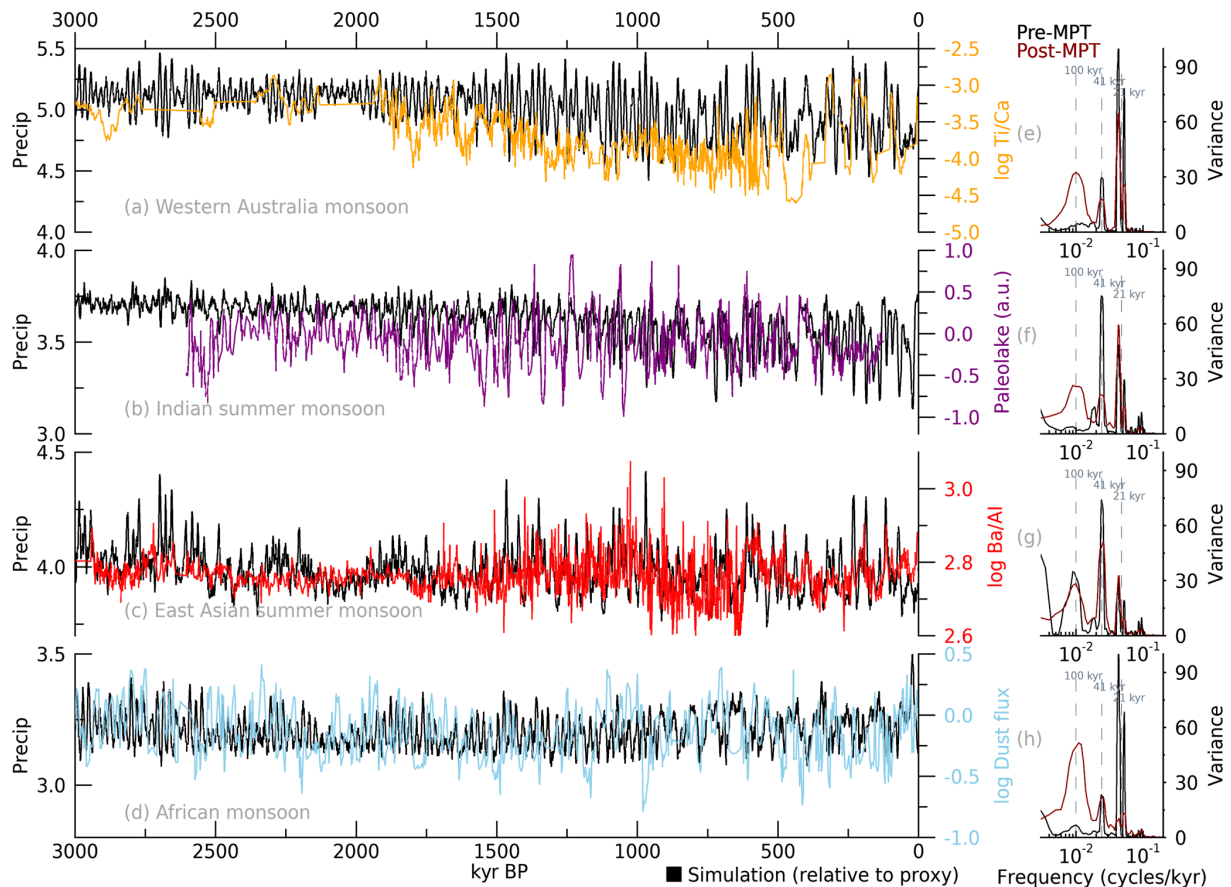
Figure 6. Global hydroclimate changes. Precipitation (unit: $\mathrm{mm\,d^{-1}}$) comparison between the proxy and simulation: **(a)** western Australia monsoon from simulation averaged over 20–5° S, 110–150° E (black) and from proxies of IODP site U1460 log Ti/Ca (Petrick et al., 2019; orange); **(b)** Indian summer monsoon from simulation averaged over 10–30° N, 70–105° E (black) and from proxies of Lake Heqing (An et al., 2011; purple); **(c)** East Asian summer monsoon from simulation averaged over 20–40° N, 110–130° E (black) and from proxies of ODP 1146 log Ba/Al (Clemens et al., 2008; red); **(d)** western African monsoon from simulation averaged over 25–5° S, 25–50° E (black) and from proxies of ODP 659 log dust flux (Tiedemann et al., 1994; sky blue). The proxy locations and respective monsoon domains are presented in Fig. S2. **(e–h)** Spectral variance of simulated pre-MPT (3–2 Ma; black) and post-MPT (1–0 Ma; brown) precipitations in western Australia monsoon **(e)**, Indian summer monsoon **(f)**, East Asian summer monsoon **(g)**, and western African monsoon **(h)**. The vertical dashed lines show 21 kyr (precession), 41 kyr (obliquity), and 100 kyr (eccentricity) periods.

certainties etc., is beyond the scope of our presentation paper here.

4   Changes in ENSO

In contrast to previous long-term transient modeling studies conducted with EMICs (Timmermann and Friedrich, 2016; Willeit et al., 2019), the CESM1.2 is capable of simulating ENSO variability and associated air–sea coupling process well, even in the coarse resolution adopted here (Liu et al., 2014) – albeit with weaker amplitude as compared to the observations. To take a broad view of the sensitivity of ENSO to external forcings over the past 3 Myr, we first show the entire monthly time series of Niño 3 index, which is defined as 1.5–7-year band-pass filtered (Liu et al., 2014) Niño 3 SST (5° S–5° N, 150–90° W) (see Fig. S4). It includes 7.2 million

monthly values. A Morlet wavelet spectrum (Torrence and Compo, 1998) of the Niño 3 SST time series (including annual cycle) (Fig. 8) reveals strong precessional-scale amplitude modulations for the annual time scale variance (i.e., averaged wavelet variance in the 0.5–1.5 year band), in agreement with recent studies (Timmermann et al., 2007; Lu et al., 2019). The annual cycle of Niño 3 SST tends to vary $\sim 90°$ out of phase with the precession index (see Fig. 5b), whereas the interannual (2–8 year) time scale wavelet variance of Niño 3 SST is in phase with the precession index (Karamperidou et al., 2020). This creates an interesting dynamic, in which variance shifts from interannual to annual timescales in response to the precessional cycle.

Furthermore, we characterize, eastern Pacific (EP) and central Pacific (CP) ENSO flavors as the standard deviation of the Niño 3 and Niño 4 (5° S–5° N, 160° E–150° W) SST
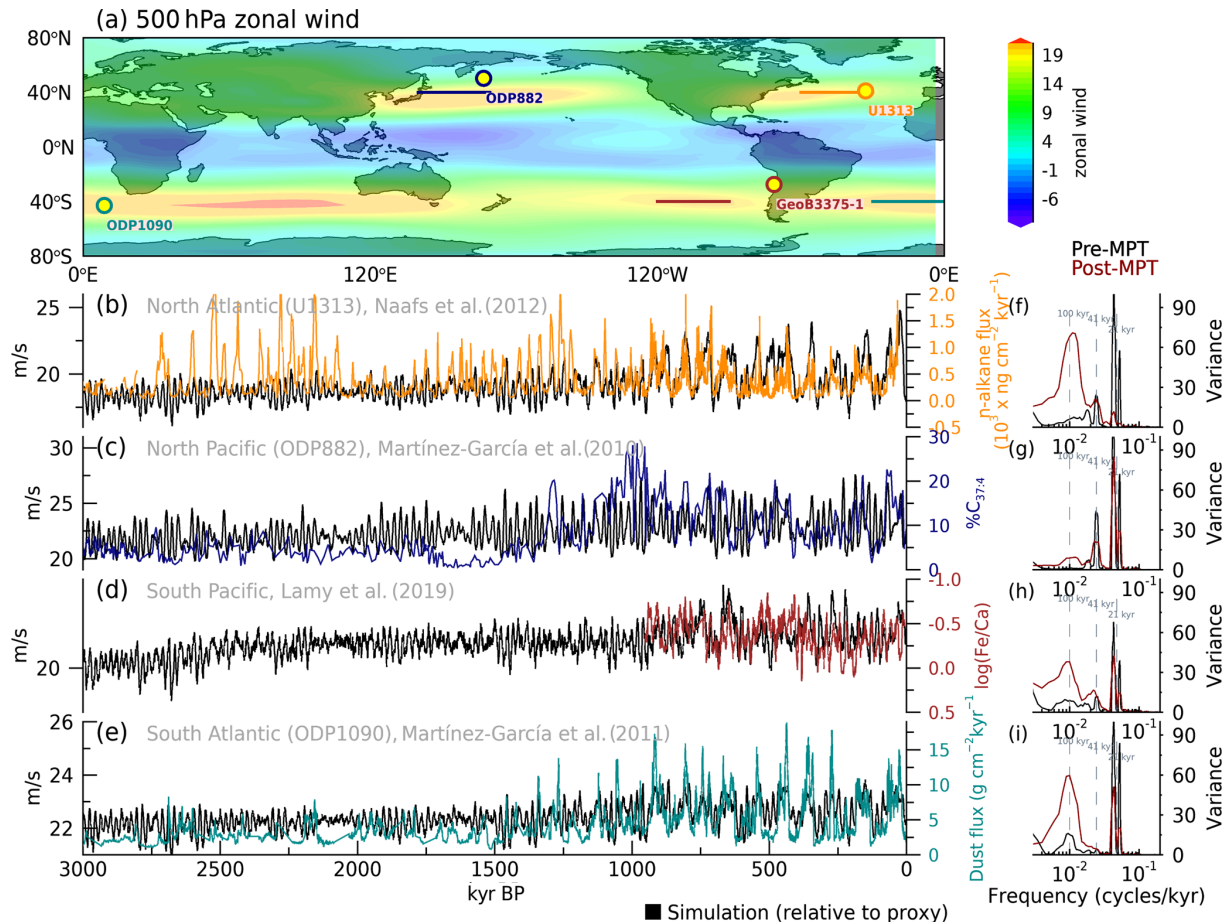
Figure 7. Global westerly wind changes. **(a)** Simulated zonal wind pattern at 500 hPa averaged for the 3 Myr period. Proxy locations and Pacific/Atlantic maximum wind regions at 40° N and 40° S are displayed in different colors. **(b–e)** Westerly comparison between the paleo-proxy data and CESM simulation (black): **(b)** North Atlantic wind from U1313 n-alkane flux (Naafs et al., 2012) and simulation (averaged over 40° N, 60–33° W). **(c)** North Pacific wind from ODP882 (Martínez-García et al., 2010) and simulation (40° N, 140–170° E), **(d)** South Pacific wind from log Fe/Ca record in fluvial sediment input (Lamy et al., 2019) and simulation (40° S, 120–90° W), and **(e)** South Atlantic wind from ODP1090 dust flux (Martínez-García et al., 2011) and simulation (40° S, 30–0° W). **(f–i)** Spectral variance of simulated pre-MPT (3–2 Ma; black) and post-MPT (1–0 Ma; brown) winds in North Atlantic **(f)**, North Pacific **(g)**, South Pacific **(h)**, and South Atlantic **(i)**. The vertical dashed lines show 21 kyr (precession), 41 kyr (obliquity), and 100 kyr (eccentricity) periods.

indices in a 1000-year window, respectively (Fig. 9a and b). We find that on precessional timescales, EP ENSO variability is in phase with CP ENSO variability and CP ENSO variability on average tends to be larger than EP ENSO variability (i.e., variability ratio shown in Fig. 9c is less than 1.0). The ratio of EP to CP ENSO variability is an indicator for how ENSO flavors change in response to orbital forcing. The ratio exhibits – apart from the precessional cycle – a strong eccentricity component with ∼ 100 and ∼ 405 kyr periodicities. The timing of the largest ratio (ratio > 2.0 and EP ENSO variability > 0.6°) occurs in ∼ 1470, ∼ 1350, ∼ 970, ∼ 230, and ∼ 130 ka. The timing in the occurrence of ENSO flavors in CESM1.2 relative to the phase of the precessional cycle is similar to that described in recent studies (e.g., Karamperidou et al., 2015). Contrary to the ENSO precessionally dominated variability, the mean state of equatorial EP SST is

largely controlled by atmospheric CO_2 variability (Fig. 9d). The different orbital characteristics of both mean state and variability suggest that the ENSO response to Milanković cycles can be attributed to the modulation of the seasonal cycle (Jin et al., 1996) rather than to changing instabilities of air–sea interactions with respect to the background state.

5 Global heat transport

Large-scale insolation and meridional temperature gradients are the main drivers for the global transport of energy. The 3 Ma simulation provides a unique opportunity to study the dominant modes of atmospheric and oceanic energy transport and their responses to orbital-scale forcings. To this end we calculated the meridional heat transport (MHT) at each
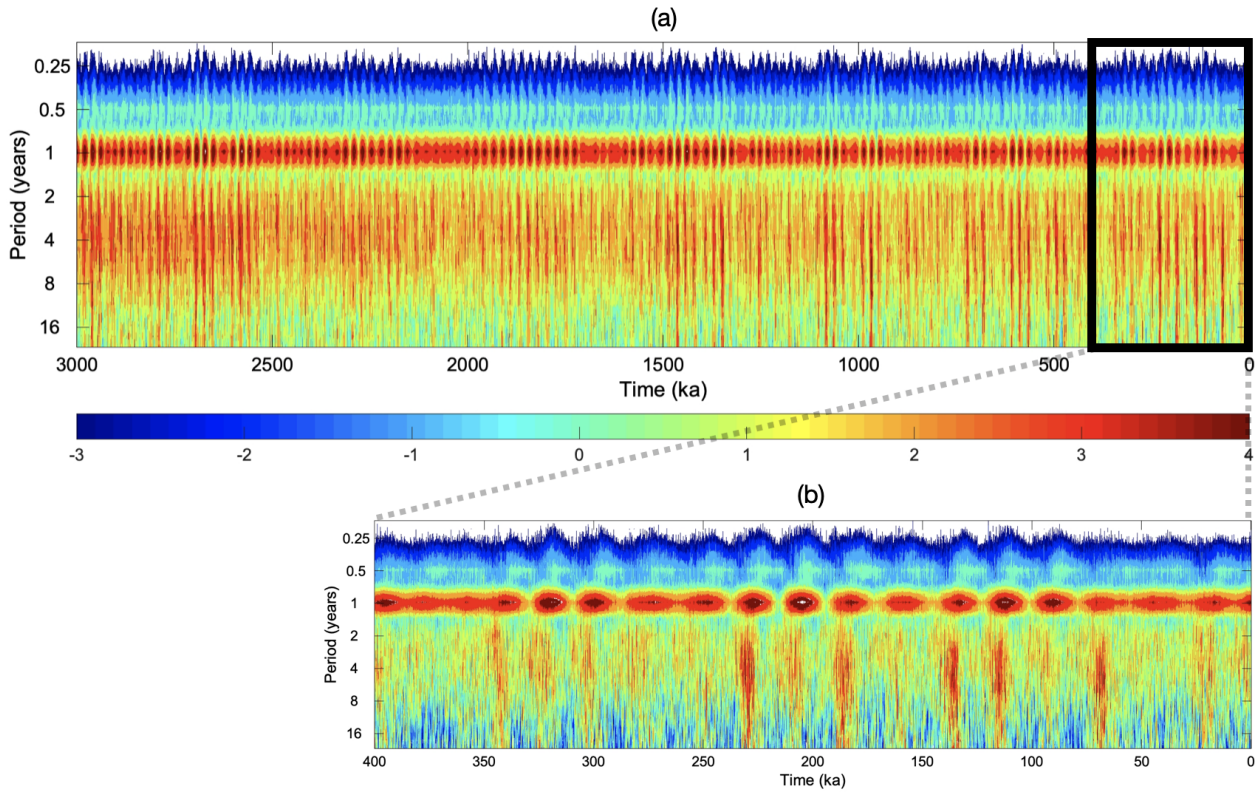
Figure 8. Monthly ENSO spectrum. Wavelet power spectrum (logarithmic variance) of Niño 3 SST (5° S–5° N, 150–90° W) during the period of **(a)** 3 Myr and **(b)** 400 kyr.
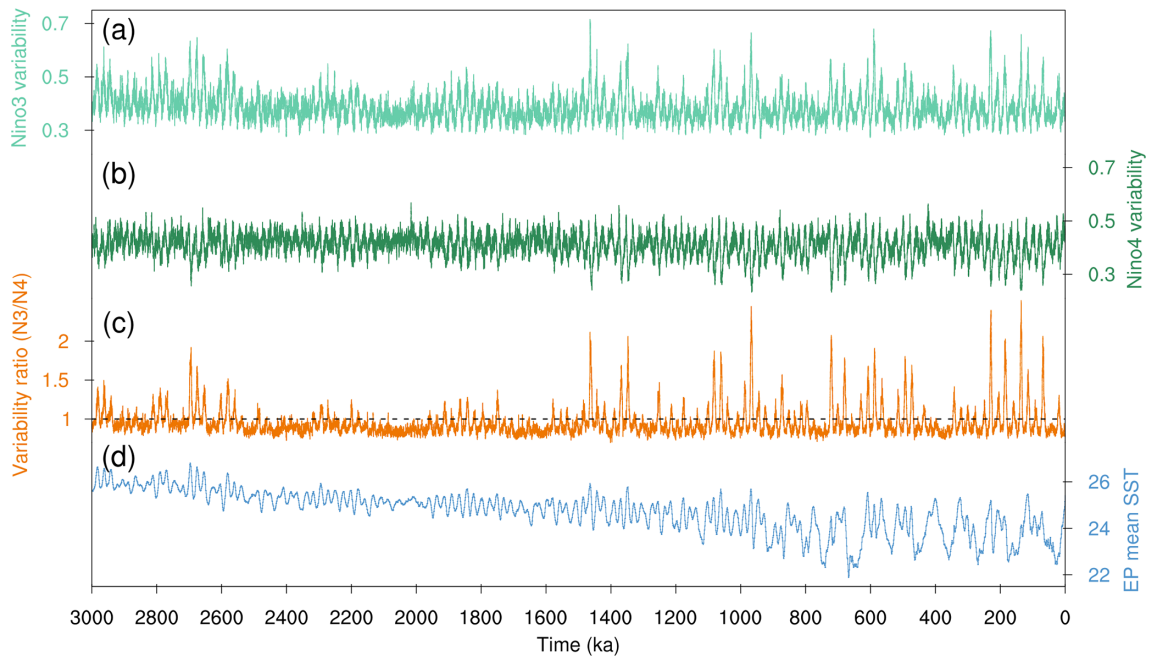

Figure 9. Comparison of monthly Niño 3 and Niño 4 variabilities. Time series of **(a)** Niño 3 SST index variability (°C), **(b)** Niño 4 SST index variability (°C), **(c)** ratio of Niño 3 variability to Niño 4 variability, and **(d)** 1000-year mean Niño 3 SST (°C). The variability in **(a, b)** was calculated as the running standard deviation of SST indices over a sliding 1000-year time window.
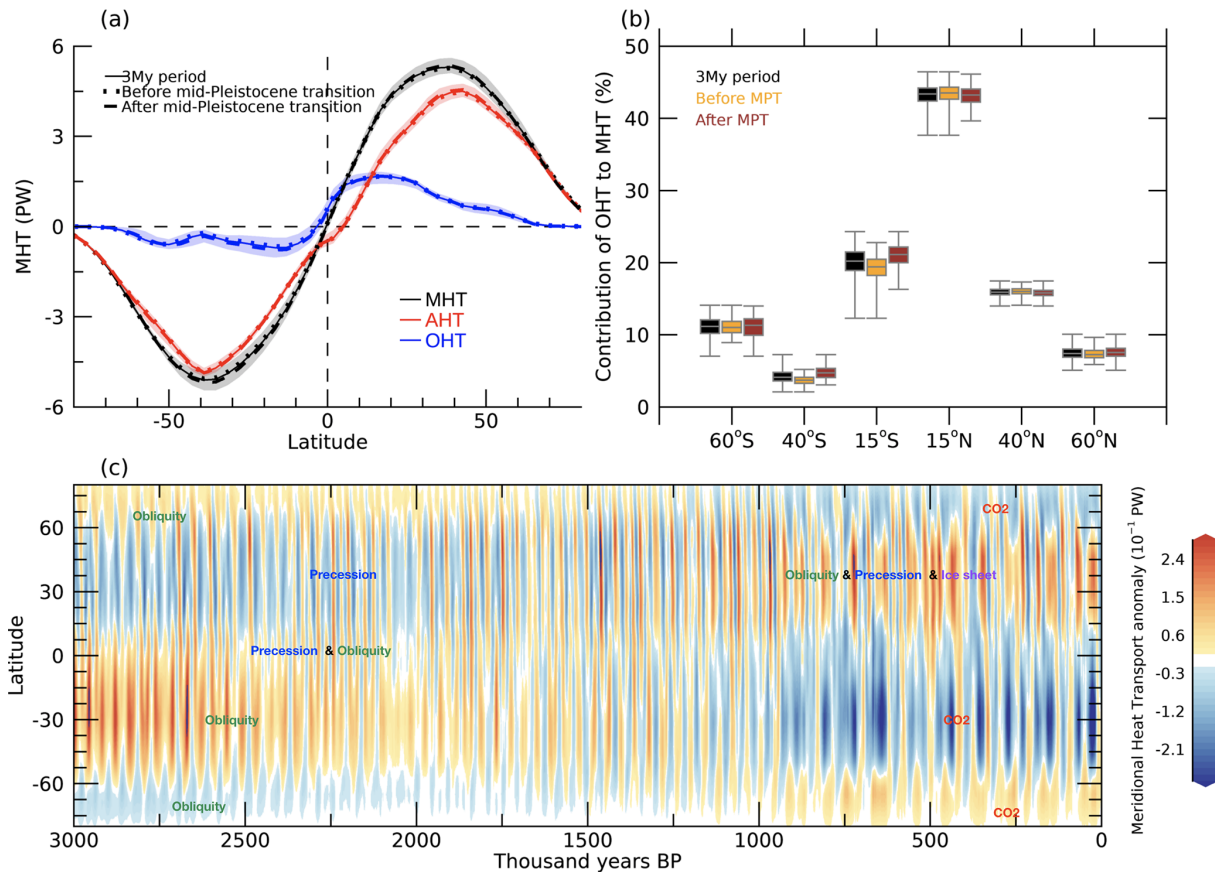
Figure 10. Global heat transport across the 3 Ma simulation. **(a)** The meridional heat transport (MHT; unit: PW; black line), atmospheric MHT (AHT; red line), and oceanic MHT (OHT; blue line) averaged over the entire 3 Myr period (solid), 41 kyr period (i.e., before the Mid-Pleistocene Transition (MPT), about 1 Ma; dotted line), and 100 kyr glacial period (i.e., after the MPT; dashed line). The minimum and maximum range of MHT changes over the 3 Myr period is displayed by corresponding color shading. **(b)** Box-whisker plot (i.e., minimum, 25 %, 50 %, 75 %, maximum range) of contribution of OHT to MHT (unit: %) at the latitude position of 60° S, 40° S, 15° S, 15° N, 40° N, and 60° N during the three different periods: the entire 3 Myr period (black), 41 kyr period (orange), and 100 kyr glacial period (brown). The contribution of AHT to MHT can be estimated by subtracting the contribution of OHT from 100 %. **(c)** The time–latitude plot of MHT anomaly (unit: 10^{-1} PW) relative to the climatological mean. Positive MHT indicates the northward heat transport.

latitude (θ), based on an energetic framework (Donohoe et al., 2020).

$$\mathrm{MHT}(\theta) = -2\pi a^2 \int\limits_{\theta}^{90} \cos(\theta)[\mathrm{ASR}(\theta) - \mathrm{OLR}(\theta)]\mathrm{d}\theta, \quad (1)$$

where ASR represents the zonal mean absorbed solar radiation and OLR denotes the zonal mean of outgoing long-wave radiation at top-of-atmosphere (TOA). The non-zero global mean values of ASR − OLR were removed from the calculation to attain energy conservation at both poles (Donohoe et al., 2020). The oceanic MHT (OHT) is directly deduced from the advection of the Eulerian mean circulation and meso-scale eddies (i.e., bolus circulation + diffusion) – the latter of which were parameterized but not explicitly resolved. There is also an indirect approach to calculate OHT using surface heat fluxes. A recent study (Yang et al., 2015) documented

the consistency between the heat transports obtained from direct and indirect approaches in the CESM. The atmospheric MHT (AHT) is then calculated as the residual of the MHT determined from TOA radiation and the OHT derived from CESM direct output. This residual approach was also applied successfully in previous studies (Donohoe et al., 2020).

Figure 10a displays the patterns of total MHT, AHT, and OHT averaged over the past 3 Myr period (solid lines). In the tropics, the MHT has strong contributions both from the atmosphere and ocean. The main sources are the atmospheric Hadley circulation and the wind-driven oceanic shallow overturning circulation in the Pacific and the deep meridional overturning circulation in the Atlantic (Schneider, 2017; Held, 2001). The poleward transport outside the tropics is mostly caused by the atmospheric eddy activity (i.e., transient eddies and stationary eddies) (e.g., Donohoe et al., 2020). Despite the coarse horizontal resolution, the

CESM1.2 captures the MHT in both atmosphere and ocean realistically (Yang et al., 2015). To further illustrate that our coarse-resolution CESM1.2 version can also capture the present-day partitioning between AHT and OHT, we compare the simulated MHTs with recent observational estimates (see Fig. A1 in Donohoe et al., 2020). The comparison reveals an overall agreement in terms of amplitude and peak latitude; however, the model exhibits a stronger AHT and weaker OHT than the observations, in agreement with previous studies (Donohoe et al., 2020; Yang et al., 2015).

In the following, we further explore the linkage between changes in the MHT (Fig. 10) and external forcings (precession, obliquity, ice sheet, and CO_2). The time–latitude changes of anomalous MHT over the past 3 Myr (Fig. 10c) show a complex spatiotemporal pattern, which documents that all forcings play an important role in controlling the MHT. For example, before the MPT, there are strong signals of both obliquity at most of the latitudes and precession in the tropics and NH mid-latitudes (particularly around 2–1 Ma), whereas after the MPT, we can see an increasing role of CO_2 on the MHTs. High obliquity values weaken the Equator-to-pole temperature gradient (Timmermann et al., 2014b) and thus affect the mid-latitude MHT, in particular prior to the MPT. Precession has a stronger impact in the tropics and NH mid-latitudes, due to the seasonally asymmetric continental responses to the precessional forcing (Merlis et al., 2013; Tigchelaar and Timmermann, 2016). The NH ice sheets alter the surface albedo and topography, thus changing the NH mid-latitude stationary and transient eddy activities (Donohoe and Battisti, 2009), whereas decreasing CO_2 concentrations enhance the southward transport of net surface heat flux toward the high latitudes of Southern Ocean (Kim, 2004).

The combined effect of these forcings leads to complex variations of the MHT by $\sim 10\%$ (0.51 PW for maximum – minimum, $1\,\mathrm{PW} = 10^{15}\,\mathrm{W}$) relative to the latitudinal maximum value of ~ 5.3 PW (see Fig. 10a). We can also see that the partitioning of the total MHT into atmospheric and oceanic contributions is time-dependent (Donohoe et al., 2020; Yu and Pritchard, 2019; Newsom et al., 2021; Liu et al., 2017). We find an increasing contribution of the Southern Ocean to the total MHT variability after the MPT (~ 1 Ma) due to the enhanced CO_2 variability (Fig. 10b), which indicates that the MPT caused the shifts in the global energy distribution and corresponding changes in regional climate feedbacks.

To further simplify the complex MHT dynamics shown in Fig. 10c, we perform an empirical orthogonal function (EOF) analysis of the zonally averaged MHT anomalies over the past 3 Myr. The principal component (PC) time series (Fig. 11a and b) of the two dominant MHT modes explain $\sim 92\%$ of the total variance. PC1 is characterized by a strong 41 kyr obliquity cycle (correlation coefficient $r \sim 0.7$ with obliquity time series) as well as a negative trend throughout the Pleistocene, whereas PC2 is more related to higher frequency variability associated with the eccentricity-

modulated precession cycle (~ 21 kyr cycle; see Fig. S5). The PC1 variability also shows a somewhat stronger 100 kyr cyclicity after the MPT. PC2 changes its overall character after the MPT, when precessional variability with an eccentricity-modulated envelope (early Pleistocene) transitions into variability which has strong eccentricity and CO_2 periodicities in the mean value (middle to late Pleistocene). We can reconfirm these characteristic changes by comparing the simulated PC2 time series with reconstructed variabilities using the precession and CO_2 forcing only (see Fig. S6). The post-MPT shift in PC1 and PC2 can be attributed mostly to the increase in the amplitude of CO_2 radiative forcing and its cyclicity (see Fig. 3c), both of which were generated from the orbitally forced climate-carbon cycle dynamics simulated by the EMIC CLIMBER-2 (Willeit et al., 2019).

The corresponding dominant MHT patterns are obtained by regressing the MHT anomalies against PC1 and PC2 (Fig. 11c and d). The PC1-related net radiation flux anomalies at the TOA and surface (Fig. 11c) show a weakening of the Equator-to-pole insolation gradient (less heat in low latitudes and more heat in high latitudes for positive PC1 values), consistent with high obliquity forcing and the effect of high CO_2 on polar amplification. The PC2-related net radiation flux anomalies (Fig. 11d) show a pronounced interhemispheric radiation gradient (i.e., warmer SH and colder NH for positive PC2). To compensate for the meridional differences of the PC1-related weakening of the Equator-to-pole net radiation gradient (Fig. 11c), an overall weakening of the poleward heat transport (i.e., anomalous northward in the SH and southward in the NH, Fig. 11e) is generated; the PC2-related strengthening of interhemispheric TOA gradient (Fig. 11d) in turn drives an anomalous northward heat transport (Fig. 11f). From these results, we define the two energy transport modes as (i) tropical heat "convergence (or divergence) mode" (PC1) and (ii) (northward or southward) "interhemispheric shift mode" (PC2), respectively. The Pleistocene global energy transport is made up by the different combinations of these two energy transport modes. The underlying processes could be accompanied by characteristic changes in both atmosphere and ocean circulations driven by NH ice-sheet albedo, sea ice albedo, and surface wind changes. The key difference between these two MHT mechanisms is associated with the orbital configuration and the response to the NH ice sheet.

6 Large-scale atmosphere and ocean circulation changes

6.1 Atmosphere

The Northern Annular Mode (NAM) and the Southern Annular Mode (SAM) are fundamental patterns of large-scale atmospheric circulation variability in both the NH and the SH. The positive phase is related to the anomalous low pressure over the polar region and high pressure over the
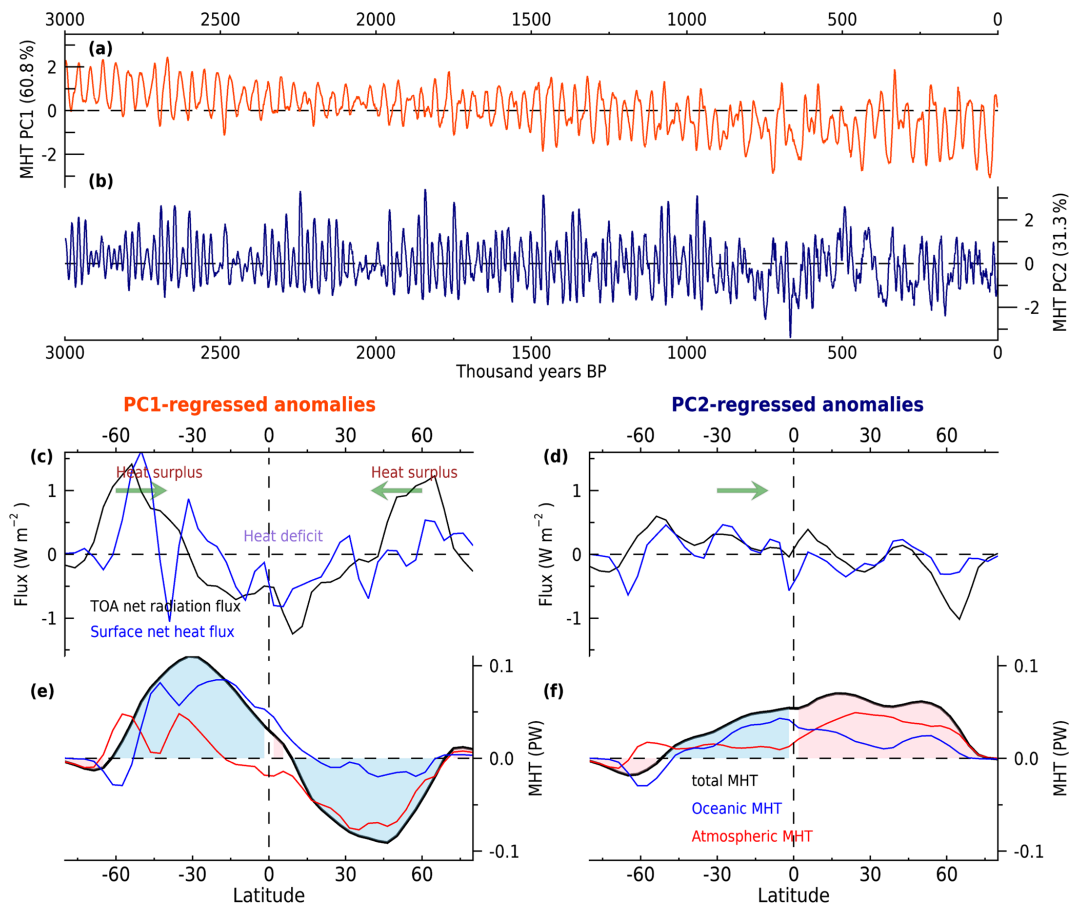
Figure 11. Spatiotemporal modes of global heat transport variability. **(a, b)** The principal component (PC) time series associated with the first two leading modes of MHT anomalies. **(c–f)** The regressed anomalies against the (left) PC1 and (right) PC2 variability: **(c, d)** zonally averaged top-of-atmosphere net radiative flux (downward in positive; unit: $W\,m^{-2}$) and surface net heat flux (toward ocean in positive; unit: $W\,m^{-2}$), **(e, f)** the total MHT (black), oceanic MHT (OHT; blue), and atmospheric MHT (AHT; red) (unit: PW). Sky-blue and pink shading in **(e, f)** indicates the weakening and strengthening of poleward total MHT, respectively.

mid-latitudes, accompanied by the strengthened (and sometimes poleward-shifted) westerly wind and storm tracks (e.g., Screen et al., 2018). We examine the variations in the NAM and SAM as key indicators for large-scale extratropical circulation changes. Figure 12 shows a strong correlation between the NAM and SAM on orbital and super-orbital timescales (correlation coefficient $r \sim 0.79$ during 3 Myr) (Fig. 12a). Both show a strong amplitude on precessional timescales before the MPT (Fig. 12b and c). However, an important difference between the NAM and SAM appears after the MPT. The post-MPT NAM has a broader spectrum band from precession (~ 21 kyr), obliquity (~ 41 kyr), to eccentricity (~ 100 kyr), which is compared with the precession-only variability of the SAM. This NAM–SAM difference may be due to the existence of NH landmass and post-MPT ice-sheet growth influencing extratropical stationary waves (Yin et al., 2008).

Compared to changes in the SAM, those in the NAM are better correlated with the major two modes of global en-

ergy transport shown in Fig. 11 (particularly for PC1-NAM, $r \sim 0.79$ during 3 Myr; $r \sim 0.44$ for PC1-SAM). For positive PC1 and negative PC2 values, the orbitally (high obliquity and low precession) driven increase of incoming insolation in high latitudes would have decreased the NH ice-sheet volume (not interactively simulated here but included implicitly in the tendency of the ice-sheet forcing). The retreat of ice sheets can weaken the large-scale circulations and stationary eddies over the NH mid-latitudes by changes in surface albedo and ice-sheet topography (Yamanouchi and Charlock, 1997). The weakening of stationary eddies leads to the reduced poleward (anomalous southward) AHT, especially in the NH mid-latitudes (see Fig. 11e). This would imply a central role of the NH large-scale circulation in modulating the global energy transport during the Pleistocene.
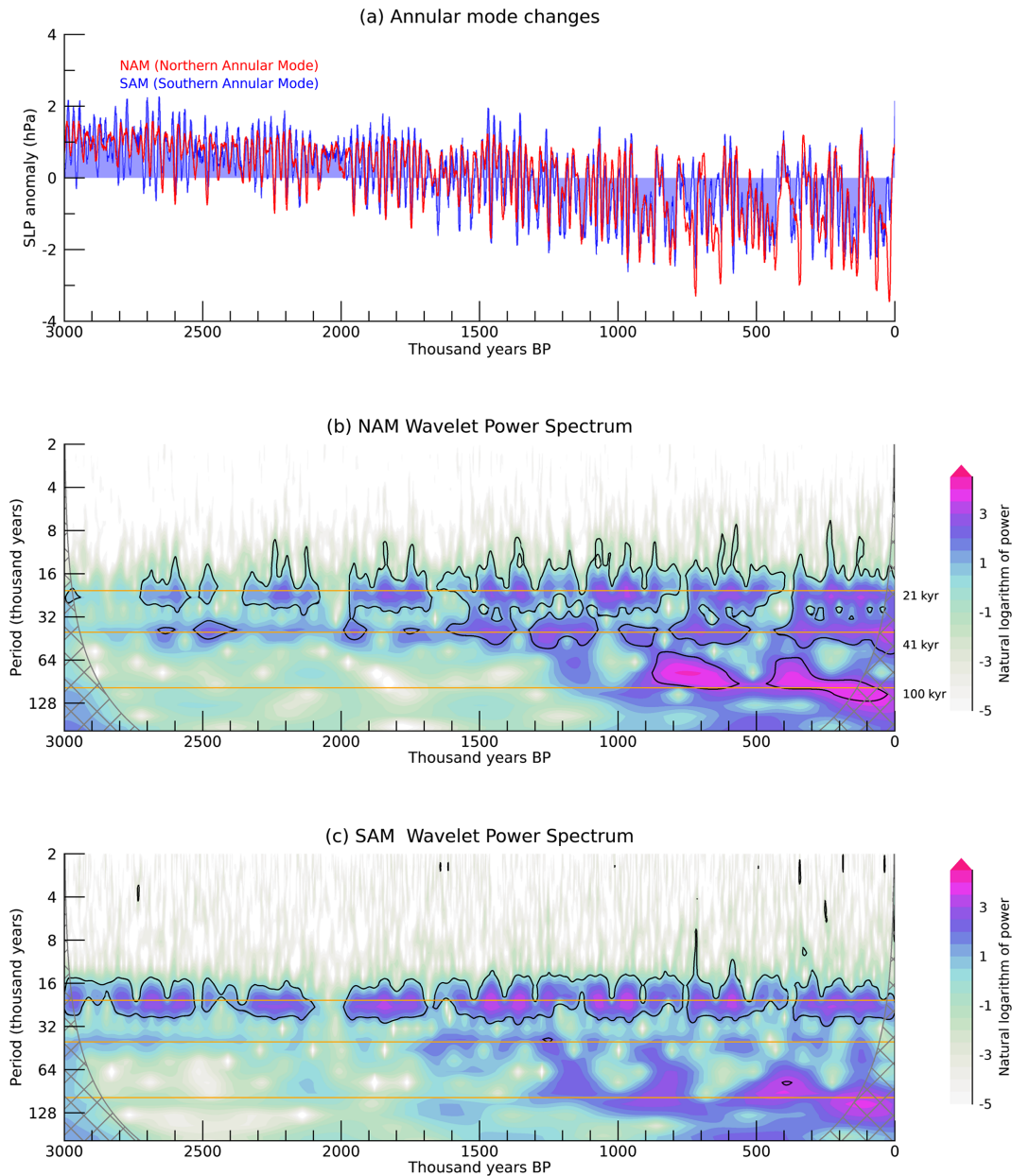
Figure 12. Atmosphere circulation changes. **(a)** The time series of Northern Annular Mode (NAM) and Southern Annular Mode (SAM). Here, the NAM is defined as the difference in zonal mean SLP at 35 and 65° N (Li and Wang, 2003) and the SAM as the difference in zonal mean SLP at 40 and 65° S (Gong and Wang, 1999). **(b, c)** The wavelet power spectrum of **(b)** NAM and **(c)** SAM indices. The black contour indicates the value significant at the 95 % confidence level. The horizonal orange lines show 21 kyr (precession), 41 kyr (obliquity), and 100 kyr (eccentricity) periods.

6.2 Ocean

Previous studies highlighted the importance of the AMOC in global energy transport (Frierson et al., 2013; Yu and Pritchard, 2019). To assess the role of ocean circulation changes in our transient simulation, we investigate the variability of the AMOC (Fig. 13a). The AMOC strength, calculated here as the maximum meridional streamfunction below 500m and north of 28° N, shows increased variabil-

ity after the MPT on precessional and obliquity timescales (Fig. 13b). Our simulation only shows weak variability on the 80–120 kyr frequency, indicating a relatively minor contribution from CO_2 and ice-sheet forcing on AMOC variability. It should be noted, however, that since our model does not include explicit meltwater forcing or calving from the ice sheets, the simulated AMOC variability on millennial and orbital timescales will be unrealistically small. In
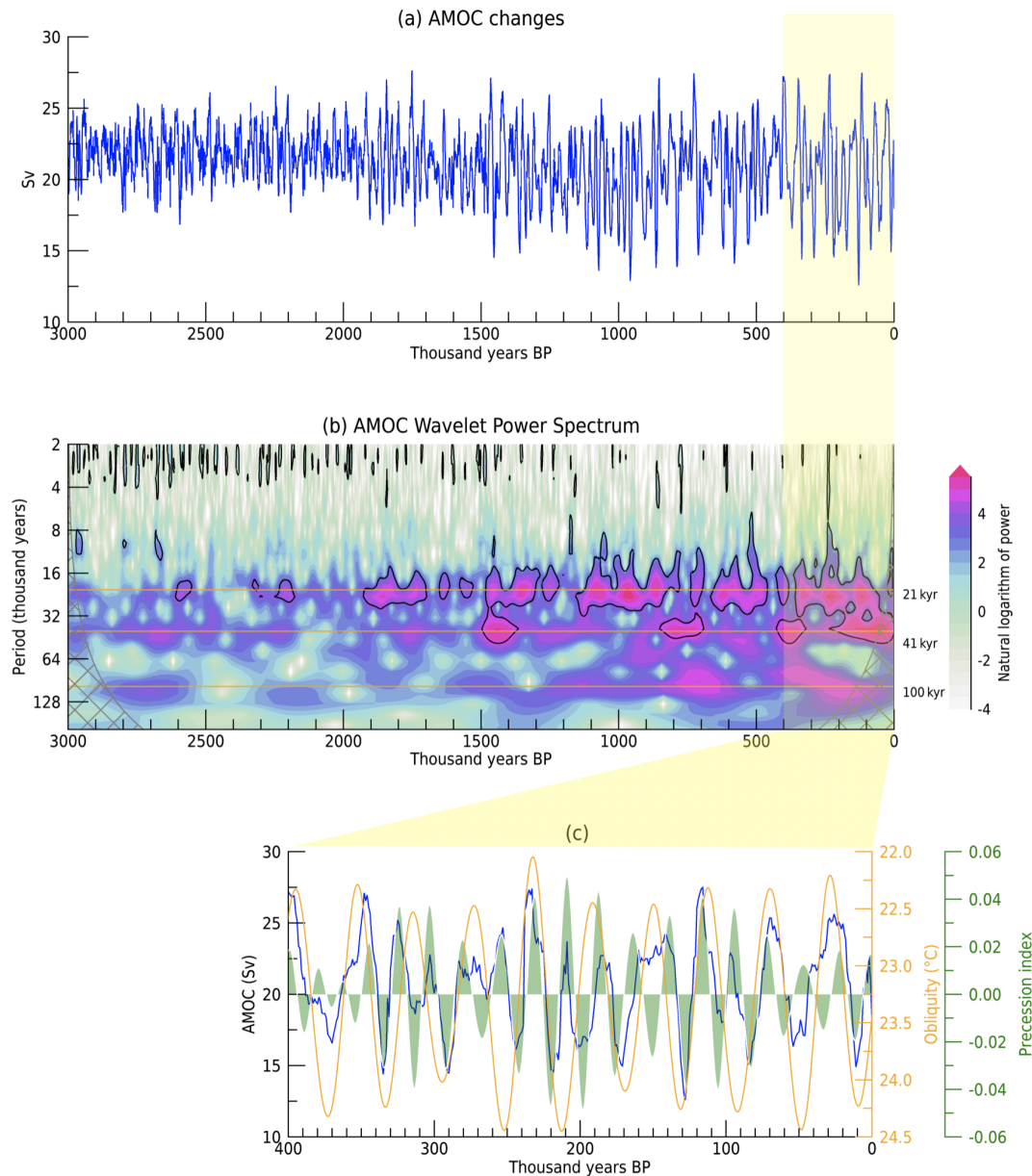
Figure 13. Ocean circulation changes. **(a)** The time series of Atlantic Meridional Overturning Circulation (AMOC). Here, the AMOC amplitude is defined as the maximum meridional stream function below 500 m and north of 28° N. **(b)** The wavelet power spectrum of AMOC amplitude. The black contour indicates the value significant at the 95 % confidence level. **(c)** 400 kyr evolution of AMOC, precession and obliquity variability. The horizonal orange lines show 21 kyr (precession), 41 kyr (obliquity), and 100 kyr (eccentricity) periods.

our simulation the AMOC amplitude varies between a minimum of 12.6 Sv to a maximum of 27.7 Sv. This result illustrates that in the absence of ice-sheet freshwater forcing, orbital forcing can play a more important role in driving an AMOC variability as compared to the GHG forcing alone (Fig. 13c). More specifically, the AMOC strength is strongly controlled by the obliquity and precession cycles associated with the two modes of global energy transport (Fig. 11). As described in Sect. 5, for a positive PC1 we find an orbitally driven weakening of the atmospheric circulation and heat transport (Fig. 11e), which also leads to a reduction in surface winds. In turn this process leads to a weakening in the NH ocean gyre circulation during high obliquity (positive PC1 in Fig. 11a). High precession values corresponding to a positive PC2 (Fig. 11b) are associated with an overall stronger AMOC and poleward heat transport (Fig. 11f). Therefore, the complex interplay between PC1 and PC2 of MHT is characterized by a modulation in the strength of the wind-driven and thermohaline ocean circulation as well as the corresponding changes in MHTs.
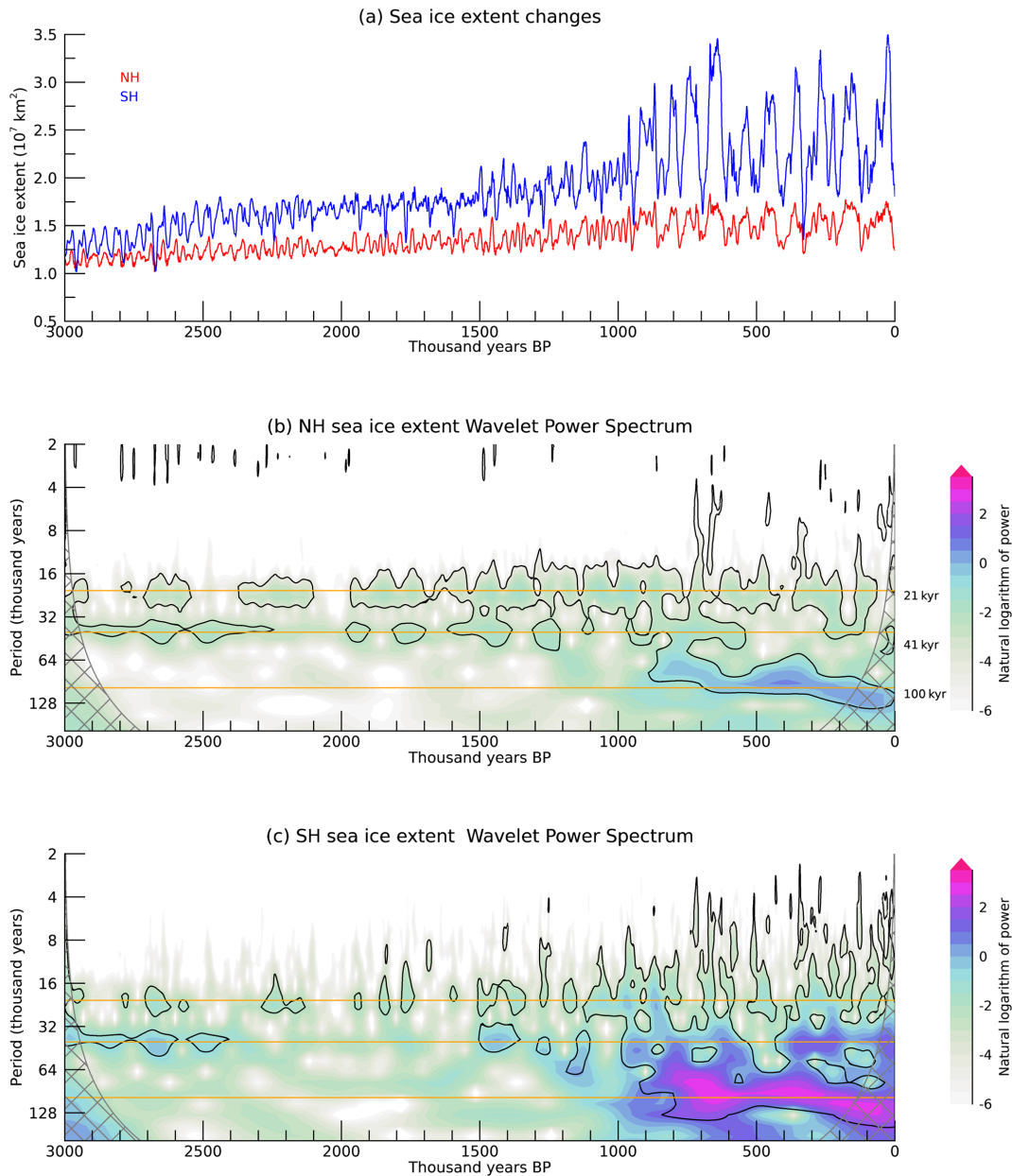
Figure 14. Sea ice changes. **(a)** The time series of sea ice extent over the Northern Hemisphere (NH, red) and Southern Hemisphere (SH, blue). **(b, c)** The wavelet power spectrum of **(b)** NH sea ice and **(c)** SH sea ice. The black contour indicates the value significant at the 95 % confidence level. The horizonal orange lines show 21 kyr (precession), 41 kyr (obliquity), and 100 kyr (eccentricity) periods.

6.3 Sea ice

To further illustrate the impact of external forcings on climate conditions, we focus on sea ice. We find a very high correlation between NH sea ice and SH sea ice ($r \sim 0.9$) (Fig. 14a). But the variance of NH sea ice extent (standard deviation of $\sim 0.16 \times 10^7\,\mathrm{km}^2$) is considerably smaller than that of SH sea ice (standard deviation of $\sim 0.43 \times 10^7\,\mathrm{km}^2$). The variability is characterized by increased spectral power on precession (~ 21 kyr), obliquity (~ 41 kyr), and CO_2/ice-sheet (~ 80–120 kyr) frequencies across the 3 Ma (Fig. 14b and c),

consistent with the combined effect of GHG and ice-sheet forcing.

Sea ice extents both in the NH and SH exhibit a pronounced post-MPT climate shift. Considering the close relationship between sea ice and mid-latitude westerlies via the modulation of the meridional temperature gradient and the atmosphere's baroclinicity (Timmermann et al., 2014b; Lamy et al., 2019; Menviel et al., 2010), we expect that the post-MPT climate shift would be more robust in the NH than the SH, due to the stronger obliquity-scale frequency

of atmospheric circulation in the NH (see Fig. 12b and c). However, the obliquity signal of sea ice extent is more pronounced in the SH. The discrepancy between both hemispheres could be primarily explained by different geographical feature: in the NH, sea ice is mostly limited to the Arctic Ocean, whereas in the SH it is unconstrained. This suggests an interesting feature of interhemispheric asymmetry for global climatic changes. For example, for high obliquity and high atmospheric CO_2 levels (positive PC1 values), the heat is transported equatorward primarily by means of the atmosphere in the NH or the ocean in the SH (see Fig. 11e). In the SH, the increased high-latitude insolation can melt more sea ice and the Southern Ocean then transports more heat through the mean equatorward Ekman transport (Morrison et al., 2016). This would reflect an increasing role of sea ice on Southern Ocean heat transport after the MPT.

7 Discussion, summary, and outlook

We presented results from the first quasi-continuous Pleistocene simulation, conducted with a CGCM, and using time-evolving forcings of the orbital parameters, GHG concentrations, and estimates of NH ice sheets. Our simulation represents well the observed orbital-scale shifts not only in the regional mean temperature changes but also in hydroclimate and large-scale westerly variabilities controlled by the earth's meridional temperature gradients. We identified a rectification mechanism by which eccentricity-modulated precessional cycles in precipitation can introduce mean state variability with periods of 100 and 405 kyr in the tropical climate system. This finding may provide a simple framework for interpreting 405 kyr eccentricity variability in long-term paleoclimatic records (Kocken et al., 2019; Nie, 2018). Simulated ENSO variability is also driven by eccentricity-modulated precessional cycles which cause an anomalous seasonal cycle forcing that interacts with ENSO. Tropical mean state changes, which are in large parts influenced by CO_2 and ice-sheet forcing, show little impact on ENSO variability and flavors.

To provide a larger context for our simulation we focused on the temporal variability of global heat transport. Two dominant modes govern the global energy transport across the 3 Ma Pleistocene: a "tropical convergence mode" related to Equator-to-pole temperature gradient and an "interhemispheric shift mode," which is linked to the interhemispheric temperature difference. These processes are accompanied by characteristic changes in both atmosphere and ocean circulations driven by westerly wind changes, the AMOC, and sea ice albedos. The two MHT modes reveal a robust regime shift for the pre- and post-MPT periods, which is most strongly pronounced for the second MHT mode. During the post-MPT glacial peaks, there is an increasing probability (from 15.3 % to 47 %) of anomalous poleward heat transport (i.e., negative PC1; colder poles than trop-

ics) and southward shifted heat transport (i.e., negative PC2; colder SH than NH), which could contribute to cooling in the NH climate and potentially an intensification of glacial conditions. We emphasize that the regime shift in the major MHT modes plays a pivotal role in reshaping the interhemispheric exchange of energy, thereby contributing to the glacial interhemispheric temperature heterogeneity and interglacial homeostasis during the late Pleistocene.

Our experimental set-up has several unrealistic features, which may impact the results in some regions: (i) we do not consider time-evolving land–sea masks due to sea level changes; (ii) freshwater forcing from the time-evolving ice sheets is not captured; (iii) the model does not include a dynamic vegetation component, nor does it explicitly simulate dust, aerosols, and climate-carbon cycle feedbacks. Using constant LGM land–sea masks throughout the entire simulation can lead to biases in regional temperature and hydroclimate and large-scale atmospheric circulation (e.g., Cao et al., 2019; Di Nezio et al., 2016). In addition, in the absence of ice-sheet-induced millennial to orbital-scale freshwater fluxes, the amplitude of AMOC variability will be underestimated compared to reality. Considering the role of AMOC changes in global energy transport (Frierson et al., 2013; Yu and Pritchard, 2019), the reduced amplitude of AMOC could alter the contribution of OHT to the MHT. The post-MPT increased variance in Southern Ocean sea ice may have further contributed to climate-carbon cycle feedbacks, which are not explicitly resolved in our simulation because we use prescribed CO_2 forcing. In a more realistic setting, which involves an interactive carbon cycle, the two MHT modes and shifts in sea ice may have influenced the outgassing of CO_2 from the ocean to atmosphere on glacial/interglacial timescales (Stein et al., 2020). For example, negative signs of PC1 and PC2 (related to Southern Ocean cooling) would amplify the Southern Ocean CO_2 sequestration, because of the increased sea ice–carbon cycle feedback and increased sinking of carbon-rich deep waters (Stott et al., 2007; Stein et al., 2020) (see Fig. S7). Thus, we hypothesize that the increased occurrence of same-sign PCs anomalies after the MPT may have helped re-enforce the glacial carbon cycle response, whereas prior to the MPT, the opposite signs of PCs may contribute partially to the compensation between CO_2 sequestration and CO_2 outgassing in the SH. Therefore, the global energy redistribution could have served as feedback in triggering glacial carbon cycle response during the late Pleistocene. Despite the limitations mentioned above, our simulation provides paleoclimate support for observational and modeling studies that link changes in atmosphere and ocean circulations to the redistribution of the global energy transport.

In this last paragraph, we will put the simulated global mean surface temperature variability over the past 3 Myr into the context of recent and future anthropogenic climate change. To this end, we ran additional simulations with the CESM1.2 model using the historical forcings (1850–
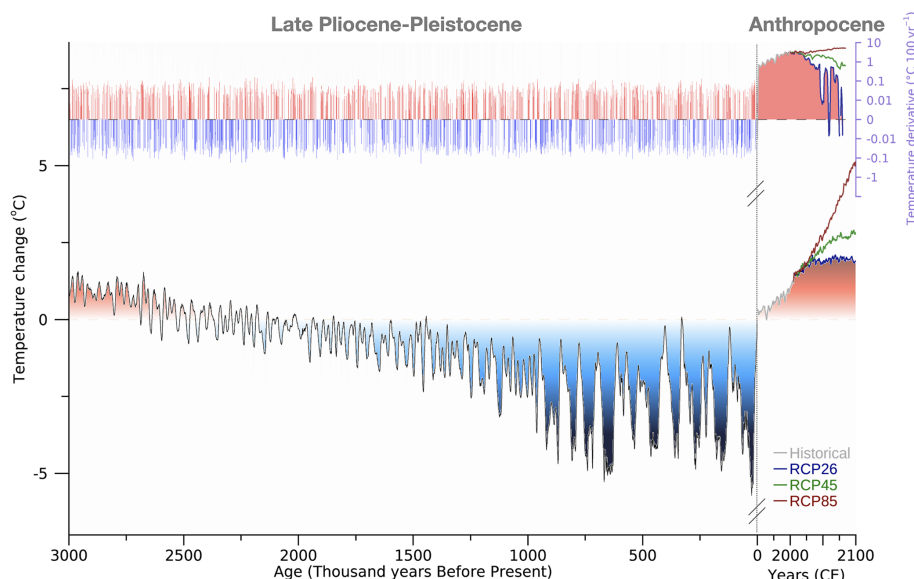
Figure 15. Past-to-future warming context. The simulated global mean surface temperature anomalies relative to 0 ka for 3 Ma and CESM1.2 simulations using historical forcings (1850–2005) and greenhouse warming scenarios following the Representative Concentration Pathway (RCP) 2.6, 4.5, and 8.5 (2006–2100). The upper panel shows the corresponding rate of global mean temperature change ($^\circ$C 100 yr^{-1}; right axis).

2005) and Representative Concentration Pathway (RCP) 2.6, 4.5 and 8.5 GHG emission scenarios (2006–2100) (Fig. 15). We find that the typical late Pleistocene glacial/interglacial temperature range of 4–6 $^\circ$C is comparable in amplitude to the RCP8.5 GHG warming projections over the next 7 decades ($\sim 5.0\,^\circ$C) (Fig. 15). In terms of warming rates ($^\circ$C 100 yr^{-1}), however, the anthropogenic projections exceed the natural variability by almost 2 orders of magnitude. This is likely to push global ecosystems way outside the range of temperature stress that they may have experienced naturally, at least within the last 3 Myr.

Some data from our quasi-continuous CESM1.2 3 Ma simulation have already been used in other studies (Margari et al., 2023; Ruan et al., 2023; Zeller et al., 2023; Timmermann et al., 2022). They have been made available on the OPeNDAP and LAS server https://climatedata.ibs.re.kr (last access: 11 October 2023) and we hope that further analyses of these runs will help in elucidating the mechanisms of past climate shifts and in the interpretation of paleoclimate proxies.

Code and data availability. The transient Pleistocene 3 Ma model data will be made available on the OPeNDAP ICCP climate data server https://climatedata.ibs.re.kr (3Ma-Data, 2023). Codes used in this study are available from the authors upon request. The code and resources for paleoclimate configuration are also available from the CESM1.2 series Paleo-climate toolkit website (https://www.cesm.ucar.edu/models/paleo , CESM1.2 Paleoclimate Toolkit, 2023). Interactive Data Language (IDL) version 8.8 was used to generate all figures.

References

Abe-Ouchi, A., Saito, F., Kawamura, K., Raymo, M. E., Okuno, J., Takahashi, K., and Blatter, H.: Insolation-driven 100,000-year glacial cycles and hysteresis of ice-sheet volume, Nature, 500, 190–193, https://doi.org/10.1038/nature12374, 2013.

An, Z., Clemens, S. C., Shen, J., Qiang, X., Jin, Z., Sun, Y., Prell, W. L., Luo, J., Wang, S., Xu, H., Cai, Y., Zhou, W., Liu, X., Liu, W., Shi, Z., Yan, L., Xiao, X., Chang, H., Wu, F., Ai, L., and Lu, F.: Glacial-Interglacial Indian Summer Monsoon Dynamics, Science, 333, 719–723, https://doi.org/10.1126/science.1203752, 2011.

An, Z., Guoxiong, W., Jianping, L., Youbin, S., Yimin, L., Weijian, Z., Yanjun, C., Anmin, D., Li, L., Jiangyu, M., Hai, C., Zheng-guo, S., Liangcheng, T., Hong, Y., Hong, A., Hong, C., and Juan, F.: Global Monsoon Dynamics and Climate Change, Annu. Rev. Earth Planet. Sci., 43, 29–77, https://doi.org/10.1146/annurev-earth-060313-054623, 2015.

Argus, D. F., Peltier, W. R., Drummond, R., and Moore, A. W.: The Antarctica component of postglacial rebound model ICE-6G_C (VM5a) based on GPS positioning, exposure age dating of ice thicknesses, and relative sea level histories, Geophys. J. Int., 198, 537–563, https://doi.org/10.1093/gji/ggu140, 2014.

Baggenstos, D., Häberli, M., Schmitt, J., Shackleton, S. A., Birner, B., Severinghaus, J. P., Kellerhals, T., and Fischer, H.: Earth's radiative imbalance from the Last Glacial Maximum to the present, P. Natl. Acad. Sci. USA, 116, 14881–14886, https://doi.org/10.1073/pnas.1905447116, 2019.

Barker, S., Knorr, G., Edwards, R. L., Parrenin, F., Putnam, A. E., Skinner, L. C., Wolff, E., and Ziegler, M.: 800,000 Years of Abrupt Climate Variability, Science, 334, 347–351, https://doi.org/10.1126/science.1203580, 2011.

Berger, A.: Long-term variations of caloric insolation resulting from the earth's orbital elements, Quatern. Res., 9, 139–167, https://doi.org/10.1016/0033-5894(78)90064-9, 1978.

Bintanja, R. and van de Wal, R. S. W.: North American ice-sheet dynamics and the onset of 100,000-year glacial cycles, Nature, 454, 869–872, https://doi.org/10.1038/nature07158, 2008.

Bjerknes, J.: Atlantic Air-Sea Interaction, in: Advances in Geophysics, edited by: Landsberg, H. E. and Van Mieghem, J., Elsevier, 1–82, https://doi.org/10.1016/S0065-2687(08)60005-9, 1964.

Cao, J., Wang, B., and Liu, J.: Attribution of the Last Glacial Maximum climate formation, Clim. Dynam., 53, 1661–1679, https://doi.org/10.1007/s00382-019-04711-6, 2019.

Cartagena-Sierra, A., Berke, M. A., Robinson, R. S., Marcks, B., Castañeda, I. S., Starr, A., Hall, I. R., Hemming, S. R., LeVay, L. J., and Party, E. S.: Latitudinal Migrations of the Subtropical Front at the Agulhas Plateau Through the Mid-Pleistocene Transition, Paleoceanogr. Paleoclim., 36, e2020PA004084, https://doi.org/10.1029/2020PA004084, 2021.

CESM1.2 Paleoclimate Toolkit: NCAR CESM1.2 code and resoures for paleoclimate configuration, https://www.cesm.ucar.edu/models/paleo (last access: 11 October 2023), 2023.

Chiang, J. C. H. and Bitz, C. M.: Influence of high latitude ice cover on the marine Intertropical Convergence Zone, Clim. Dynam., 25, 477–496, https://doi.org/10.1007/s00382-005-0040-5, 2005.

Clark, P. U., Archer, D., Pollard, D., Blum, J. D., Rial, J. A., Brovkin, V., Mix, A. C., Pisias, N. G., and Roy, M.: The middle Pleistocene transition: characteristics, mechanisms, and implications for long-term changes in atmospheric pCO$_2$, Quaternary Sci. Rev., 25, 3150–3184, https://doi.org/10.1016/j.quascirev.2006.07.008, 2006.

Clemens, S. C. and Prell, W. L.: A 350,000 year summer-monsoon multi-proxy stack from the Owen Ridge, Northern Arabian Sea, Mar. Geol., 201, 35–51, https://doi.org/10.1016/S0025-3227(03)00207-X, 2003.

Clemens, S. C., Prell, W. L., Sun, Y., Liu, Z., and Chen, G.: Southern Hemisphere forcing of Pliocene δ^{18}O and the evolution of Indo-Asian monsoons, Paleoceanography, 23, PA4210, https://doi.org/10.1029/2008PA001638, 2008.

Clemens, S. C., Holbourn, A., Kubota, Y., Lee, K. E., Liu, Z., Chen, G., Nelson, A., and Fox-Kemper, B.: Precession-band variance missing from East Asian monsoon runoff, Nat. Commun., 9, 3364, https://doi.org/10.1038/s41467-018-05814-0, 2018.

Clement, A. C., Hall, A., and Broccoli, A. J.: The importance of precessional signals in the tropical climate, Clim. Dynam., 22, 327–341, https://doi.org/10.1007/s00382-003-0375-8, 2004.

Davis, B. A. S. and Brewer, S.: Orbital forcing and role of the latitudinal insolation/temperature gradient, Clim. Dynam. 32, 143–165, https://doi.org/10.1007/s00382-008-0480-9, 2009.

de Garidel-Thoron, T., Rosenthal, Y., Bassinot, F., and Beaufort, L.: Stable sea surface temperatures in the western Pacific warm pool over the past 1.75 million years, Nature, 433, 294–298, https://doi.org/10.1038/nature03189, 2005.

Di Nezio, P. N., Timmermann, A., Tierney, J. E., Jin, F. F., Otto-Bliesner, B., Rosenbloom, N., Mapes, B., Neale, R., Ivanovic, R. F., and Montenegro, A.: The climate response of the Indo-Pacific warm pool to glacial sea level, Paleoceanography, 31, 866–894, https://doi.org/10.1002/2015pa002890, 2016.

Donohoe, A. and Battisti, D. S.: Causes of Reduced North Atlantic Storm Activity in a CAM3 Simulation of the Last Glacial Maximum, J. Climate, 22, 4793–4808, https://doi.org/10.1175/2009jcli2776.1, 2009.

Donohoe, A., Armour, K. C., Roe, G. H., Battisti, D. S., and Hahn, L.: The Partitioning of Meridional Heat Transport from the Last Glacial Maximum to CO$_2$ Quadrupling in Coupled Climate Models, J. Climate, 33, 4141–4165, https://doi.org/10.1175/jcli-d-19-0797.1, 2020.

Friedrich, T. and Timmermann, A.: Millennial-scale glacial meltwater pulses and their effect on the spatiotemporal benthic δ^{18}O variability, Paleoceanography, 27, PA3215, https://doi.org/10.1029/2012pa002330, 2012.

Friedrich, T., Timmermann, A., Tigchelaar, M., Timm, O. E., and Ganopolski, A.: Nonlinear climate sensitivity and its implications for future greenhouse warming, Sci. Adv., 2, e1501923, https://doi.org/10.1126/sciadv.1501923, 2016.

Frierson, D. M. W., Hwang, Y.-T., Fučkar, N. S., Seager, R., Kang, S. M., Donohoe, A., Maroon, E. A., Liu, X., and Battisti, D. S.: Contribution of ocean overturning circulation to tropical rainfall peak in the Northern Hemisphere, Nat. Geosci., 6, 940–944, https://doi.org/10.1038/ngeo1987, 2013.

Ganopolski, A., Calov, R., and Claussen, M.: Simulation of the last glacial cycle with a coupled climate ice-sheet model of intermediate complexity, Clim. Past, 6, 229–244, https://doi.org/10.5194/cp-6-229-2010, 2010.

Gong, D. and Wang, S.: Definition of Antarctic Oscillation index, Geophys. Res. Lett., 26, 459–462, https://doi.org/10.1029/1999GL900003, 1999.

Goosse, H., Brovkin, V., Fichefet, T., Haarsma, R., Huybrechts, P., Jongma, J., Mouchet, A., Selten, F., Barriat, P. Y., Campin, J. M., Deleersnijder, E., Driesschaert, E., Goelzer, H., Janssens, I., Loutre, M. F., Morales Maqueda, M. A., Opsteegh, T., Mathieu, P. P., Munhoven, G., Pettersson, E. J., Renssen, H., Roche, D. M., Schaeffer, M., Tartinville, B., Timmermann, A., and Weber, S. L.: Description of the Earth system model of intermediate complexity LOVECLIM version 1.2, Geosci. Model Dev., 3, 603–633, https://doi.org/10.5194/gmd-3-603-2010, 2010.

Hahn, L. C., Armour, K. C., Battisti, D. S., Donohoe, A., Pauling, A. G., and Bitz, C. M.: Antarctic Elevation Drives Hemispheric Asymmetry in Polar Lapse Rate Climatology and Feedback, Geophys. Res. Lett., 47, e2020GL088965, https://doi.org/10.1029/2020GL088965, 2020.

Heinemann, M., Timmermann, A., Timm, O. E., Saito, F., and Abe-Ouchi, A.: Deglacial ice sheet meltdown: orbital pacemaking and CO_2 effects, Clim. Past, 10, 1567–1579, https://doi.org/10.5194/cp-10-1567-2014, 2014.

Held, I. M.: The Partitioning of the Poleward Energy Transport between the Tropical Ocean and Atmosphere, J. Atmos. Sci., 58, 943–948, https://doi.org/10.1175/1520-0469(2001)058<0943:Tpotpe>2.0.Co;2, 2001.

Herbert, T. D., Peterson, L. C., Lawrence, K. T., and Liu, Z.: Tropical Ocean Temperatures Over the Past 3.5 Million Years, Science, 328, 1530–1534, https://doi.org/10.1126/science.1185435, 2010.

Hu, A., Meehl, G., Han, W., Timmermann, A., Otto-Bliesner, B., Liu, Z., Washington, W., Large, W., Abe-Ouchi, A., Kimoto, M., Lambeck, K., and Wu, B.: Role of the Bering Strait on the hysteresis of the ocean conveyor belt circulation and glacial climate stability, P. Natl. Acad. Sci. USA, 109, 6417–6422, https://doi.org/10.1073/pnas.1116014109, 2012.

Hurrell, J. W., Holland, M. M., Gent, P. R., Ghan, S., Kay, J. E., Kushner, P. J., Lamarque, J.-F., Large, W. G., Lawrence, D., Lindsay, K., Lipscomb, W. H., Long, M. C., Mahowald, N., Marsh, D. R., Neale, R. B., Rasch, P., Vavrus, S., Vertenstein, M., Bader, D., Collins, W. D., Hack, J. J., Kiehl, J., and Marshall, S.: The Community Earth System Model: A Framework for Collaborative Research, B. Am. Meteorol. Soc., 94, 1339–1360, https://doi.org/10.1175/bams-d-12-00121.1, 2013.

Jin, F. F., Neelin, J. D., and Ghil, M.: El Nino Southern Oscillation and the annual cycle: Subharmonic frequency-locking and aperiodicity, Physica D, 98, 442–465, https://doi.org/10.1016/0167-2789(96)00111-x, 1996.

Johnson, T. C., Werne, J. P., Brown, E. T., Abbott, A., Berke, M., Steinman, B. A., Halbur, J., Contreras, S., Grosshuesch, S., Deino, A., Scholz, C. A., Lyons, R. P., Schouten, S., and Damsté, J. S. S.: A progressively wetter climate in southern East Africa over the past 1.3 million years, Nature, 537, 220–224, https://doi.org/10.1038/nature19065, 2016.

Jouzel, J., Masson-Delmotte, V., Cattani, O., Dreyfus, G., Falourd, S., Hoffmann, G., Minster, B., Nouet, J., Barnola, J. M., Chappellaz, J., Fischer, H., Gallet, J. C., Johnsen, S., Leuenberger, M., Loulergue, L., Luethi, D., Oerter, H., Parrenin, F., Raisbeck, G., Raynaud, D., Schilt, A., Schwander, J., Selmo, E., Souchez, R., Spahni, R., Stauffer, B., Steffensen, J. P., Stenni, B., Stocker, T. F., Tison, J. L., Werner, M., and Wolff, E. W.: Orbital and Millennial Antarctic Climate Variability over the Past 800,000 Years, Science, 317, 793–796, https://doi.org/10.1126/science.1141038, 2007.

Kamae, Y., Yoshida, K., and Ueda, H.: Sensitivity of Pliocene climate simulations in MRI-CGCM2.3 to respective boundary conditions, Clim. Past, 12, 1619–1634, https://doi.org/10.5194/cp-12-1619-2016, 2016.

Kang, S. M., Shin, Y., and Xie, S.-P.: Extratropical forcing and tropical rainfall distribution: energetics framework and ocean Ekman advection, npj Clim. Atmos. Sci., 1, 20172, https://doi.org/10.1038/s41612-017-0004-6, 2018.

Karamperidou, C., Di Nezio, P. N., Timmermann, A., Jin, F. F., and Cobb, K. M.: The response of ENSO flavors to mid-Holocene climate: implications for proxy interpretation, Paleoceanography, 30, 527–547, 2015.

Karamperidou, C., Stuecker, M. F., Timmermann, A., Yun, K.-S., Lee, S.-S., Jin, F. F., Santoso, A., McPhaden, M. J., and Cai, W.: ENSO in a Changing Climate: Challenges, Paleo-Perspectives, and Outlook, in: El Niño Southern Oscillation in a Changing Climate, edited by: McPhaden, M. J., Santoso, A., and Cai, W., John Wiley & Sons, Inc., 471–484, https://doi.org/10.1002/9781119548164.ch21, 2020.

Kaspar, F., Spangehl, T., and Cubasch, U.: Northern hemisphere winter storm tracks of the Eemian interglacial and the last glacial inception, Clim. Past, 3, 181–192, https://doi.org/10.5194/cp-3-181-2007, 2007.

Kim, S. J.: The effect of atmospheric CO_2 and ice sheet topography on LGM climate, Clim. Dynam., 22, 639–651, https://doi.org/10.1007/s00382-004-0412-2, 2004.

Kindler, P., Guillevic, M., Baumgartner, M., Schwander, J., Landais, A., and Leuenberger, M.: Temperature reconstruction from 10 to 120 kyr b2k from the NGRIP ice core, Clim. Past, 10, 887–902, https://doi.org/10.5194/cp-10-887-2014, 2014.

Kocken, I. J., Cramwinckel, M. J., Zeebe, R. E., Middelburg, J. J., and Sluijs, A.: The 405 kyr and 2.4 Myr eccentricity components in Cenozoic carbon isotope records, Clim. Past, 15, 91–104, https://doi.org/10.5194/cp-15-91-2019, 2019.

Kohler, P., Bintanja, R., Fischer, H., Joos, F., Knutti, R., Lohmann, G., and Masson-Delmotte, V.: What caused Earth's temperature variations during the last 800,000 years? Data-based evidence on radiative forcing and constraints on climate sensitivity, Quaternary Sci. Rev., 29, 129–145, https://doi.org/10.1016/j.quascirev.2009.09.026, 2010.

Kutzbach, J. E. and Guetter, P. J.: The Influence of Changing Orbital Parameters and Surface Boundary Conditions on Climate Simulations for the Past 18 000 Years, J. Atmos. Sci., 43, 1726–1759, https://doi.org/10.1175/1520-0469(1986)043<1726:Tiocop>2.0.Co;2, 1986.

Lamy, F., Chiang, J. C. H., Martínez-Méndez, G., Thierens, M., Arz, H. W., Bosmans, J., Hebbeln, D., Lambert, F., Lembke-Jene, L., and Stuut, J.-B.: Precession modulation of the South Pacific westerly wind belt over the past million years, P. Natl. Acad. Sci. USA, 116, 23455–23460, https://doi.org/10.1073/pnas.1905847116, 2019.

Laskar, J., Robutel, P., Joutel, F., Gastineau, M., Correia, A. C. M., and Levrard, B.: A long-term numerical solution for the insolation quantities of the Earth, Astron. Astrophys., 428, 261–285, 2004.

Lawrence, K. T., Herbert, T. D., Brown, C. M., Raymo, M. E., and Haywood, A. M.: High-amplitude variations in North Atlantic sea surface temperature during the early Pliocene warm period, Paleoceanography, 24, PA2218, https://doi.org/10.1029/2008PA001669, 2009.

Li, J. and Wang, J. X. L.: A modified zonal index and its physical sense, Geophys. Res. Lett., 30, 1632, https://doi.org/10.1029/2003GL017441, 2003.

Lilien, D. A., Steinhage, D., Taylor, D., Parrenin, F., Ritz, C., Mulvaney, R., Martin, C., Yan, J. B., O'Neill, C., Frezzotti, M., Miller, H., Gogineni, P., Dahl-Jensen, D., and Eisen, O.: Brief communication: New radar constraints support presence of ice older than 1.5 Myr at Little Dome C, The Cryosphere, 15, 1881–1888, https://doi.org/10.5194/tc-15-1881-2021, 2021.

Lisiecki, L. E. and Raymo, M. E.: A Pliocene-Pleistocene stack of 57 globally distributed benthic δ^{18}O records, Paleoceanography, 20, PA1003, https://doi.org/10.1029/2004PA001071, 2005.

Liu, X., Battisti, D. S., and Donohoe, A.: Tropical Precipitation and Cross-Equatorial Ocean Heat Transport during the Mid-Holocene, J. Climate, 30, 3529–3547, https://doi.org/10.1175/jcli-d-16-0502.1, 2017.

Liu, Y., Lo, L., Shi, Z., Wei, K.-Y., Chou, C.-J., Chen, Y.-C., Chuang, C.-K., Wu, C.-C., Mii, H.-S., Peng, Z., Amakawa, H., Burr, G. S., Lee, S.-Y., DeLong, K. L., Elderfield, H., and Shen, C.-C.: Obliquity pacing of the western Pacific Intertropical Convergence Zone over the past 282,000 years, Nat. Commun., 6, 10018, https://doi.org/10.1038/ncomms10018, 2015.

Liu, Z., Otto-Bliesner, B. L., He, F., Brady, E. C., Tomas, R., Clark, P. U., Carlson, A. E., Lynch-Stieglitz, J., Curry, W., Brook, E., Erickson, D., Jacob, R., Kutzbach, J., and Cheng, J.: Transient Simulation of Last Deglaciation with a New Mechanism for Bølling-Allerød Warming, Science, 325, 310–314, https://doi.org/10.1126/science.1171041, 2009.

Liu, Z., Lu, Z., Wen, X., Otto-Bliesner, B. L., Timmermann, A., and Cobb, K. M.: Evolution and forcing mechanisms of El Niño over the past 21,000 years, Nature, 515, 550–553, 2014.

Lorenz, S. J. and Lohmann, G.: Acceleration technique for Milankovitch type forcing in a coupled atmosphere-ocean circulation model: method and application for the holocene, Clim. Dynam., 23, 727–743, https://doi.org/10.1007/s00382-004-0469-y, 2004.

Lu, Z., Liu, Z., Chen, G., and Guan, J.: Prominent precession band variance in ENSO intensity over the last 300,000 years, Geophys. Res. Lett., 46, 9786–9795, 2019.

Lunt, D. J., Williamson, M. S., Valdes, P. J., Lenton, T. M., and Marsh, R.: Comparing transient, accelerated, and equilibrium simulations of the last 30 000 years with the GENIE-1 model, Clim. Past, 2, 221–235, https://doi.org/10.5194/cp-2-221-2006, 2006.

Lupien, R. L., Russell, J. M., Pearson, E. J., Castañeda, I. S., Asrat, A., Foerster, V., Lamb, H. F., Roberts, H. M., Schäbitz, F., Trauth, M. H., Beck, C. C., Feibel, C. S., and Cohen, A. S.: Orbital controls on eastern African hydroclimate in the Pleistocene, Sci. Rep.-UK, 12, 3170, https://doi.org/10.1038/s41598-022-06826-z, 2022.

Lüthi, D., Le Floch, M., Bereiter, B., Blunier, T., Barnola, J.-M., Siegenthaler, U., Raynaud, D., Jouzel, J., Fischer, H., Kawamura, K., and Stocker, T. F.: High-resolution carbon dioxide concentration record 650,000–800,000 years before present, Nature, 453, 379–382, https://doi.org/10.1038/nature06949, 2008.

Margari, V., Hodell, D. A., Parfitt, S. A., Ashton, N. M., Grimalt, J. O., Kim, H., Yun, K.-S., Gibbard, P. L., Stringer, C. B., Timmermann, A., and Tzedakis, P. C.: Extreme glacial cooling likely led to hominin depopulation of Europe in the Early Pleistocene, Science, 381, 693–699, https://doi.org/10.1126/science.adf4445, 2023.

Martínez-Garcia, A., Rosell-Melé, A., McClymont, E. L., Gersonde, R., and Haug, G. H.: Subpolar Link to the Emergence of the Modern Equatorial Pacific Cold Tongue, Science, 328, 1550–1553, https://doi.org/10.1126/science.1184480, 2010.

Martínez-Garcia, A., Rosell-Melé, A., Jaccard, S. L., Geibert, W., Sigman, D. M., and Haug, G. H.: Southern Ocean dust–climate coupling over the past four million years, Nature, 476, 312–315, https://doi.org/10.1038/nature10310, 2011.

Masson-Delmotte, V., Schulz, M., Abe-Ouchi, A., Beer, J., Ganopolski, A., González Rouco, J. F., Jansen, E., Lambeck, K., Luterbacher, J., Naish, T., Osborn, T., Otto-Bliesner, B., Quinn, T., Ramesh, R., Rojas, M., Shao, X., and Timmermann, A.: Information from paleoclimate archives, in: Climate Change 2013: The Physical Science Basis, Contribution of Working Group I to the Fifth Assessment Report of the Intergovernmental Panel on Climate Change, edited by: Stocker, T. F., Qin, D., Plattner, G.-K., Tignor, M., Allen, S. K., Doschung, J., Nauels, A., Xia, Y., Bex, V., and Midgley, P. M., Cambridge University Press, 383–464, https://doi.org/10.1017/cbo9781107415324.013, 2013.

McClymont, E. L., Sosdian, S. M., Rosell-Melé, A., and Rosenthal, Y.: Pleistocene sea-surface temperature evolution: Early cooling, delayed glacial intensification, and implications for the mid-Pleistocene climate transition, Earth-Sci. Rev., 123, 173–193, https://doi.org/10.1016/j.earscirev.2013.04.006, 2013.

Meehl, G. A., Senior, C. A., Eyring, V., Flato, G., Lamarque, J.-F., Stouffer, R. J., Taylor, K. E., and Schlund, M.: Context for interpreting equilibrium climate sensitivity and transient climate response from the CMIP6 Earth system models, Sci. Adv., 6, eaba1981, https://doi.org/10.1126/sciadv.aba1981, 2020.

Menviel, L., Timmermann, A., Timm, O. E., and Mouchet, A.: Climate and biogeochemical response to a rapid melting of the West Antarctic Ice Sheet during interglacials and implications for future climate, Paleoceanography, 25, PA4231, https://doi.org/10.1029/2009pa001892, 2010.

Menviel, L., Timmermann, A., Timm, O. E., and Mouchet, A.: Deconstructing the Last Glacial termination: the role of millennial and orbital-scale forcings, Quaternary Sci. Rev., 30, 1155–1172, https://doi.org/10.1016/j.quascirev.2011.02.005, 2011.

Menviel, L., Timmermann, A., Friedrich, T., and England, M. H.: Hindcasting the continuum of Dansgaard-Oeschger variability: mechanisms, patterns and timing, Clim. Past, 10, 63–77, https://doi.org/10.5194/cp-10-63-2014, 2014.

Merlis, T. M., Schneider, T., Bordoni, S., and Eisenman, I.: Hadley Circulation Response to Orbital Precession. Part II: Subtropical Continent, J. Climate, 26, 754–771, https://doi.org/10.1175/jcli-d-12-00149.1, 2013.

Morrison, A. K., Griffies, S. M., Winton, M., Anderson, W. G., and Sarmiento, J. L.: Mechanisms of Southern Ocean Heat Uptake

and Transport in a Global Eddying Climate Model, J. Climate, 29, 2059–2075, https://doi.org/10.1175/jcli-d-15-0579.1, 2016.

Naafs, B. D. A., Hefter, J., Acton, G., Haug, G. H., Martínez-Garcia, A., Pancost, R., and Stein, R.: Strengthening of North American dust sources during the late Pliocene (2.7 Ma), Earth Planet. Sc. Lett., 317–318, 8–19, https://doi.org/10.1016/j.epsl.2011.11.026, 2012.

Newsom, E. R., Thompson, A. F., Adkins, J. F., and Galbraith, E. D.: A hemispheric asymmetry in poleward ocean heat transport across climates: Implications for overturning and polar warming, Earth Planet. Sc. Lett., 568, 117033, https://doi.org/10.1016/j.epsl.2021.117033, 2021.

Nie, J. S.: The Plio-Pleistocene 405-kyr climate cycles, Palaeogeogr. Palaeocl. Palaeoecol., 510, 26–30, https://doi.org/10.1016/j.palaeo.2017.07.022, 2018.

Petrick, B., Martínez-García, A., Auer, G., Reuning, L., Auderset, A., Deik, H., Takayanagi, H., De Vleeschouwer, D., Iryu, Y., and Haug, G. H.: Glacial Indonesian Throughflow weakening across the Mid-Pleistocene Climatic Transition, Sci. Rep.-UK, 9, 16995, https://doi.org/10.1038/s41598-019-53382-0, 2019.

Ruan, J., Timmermann, A., Raia, P., Yun, K.-S., Zeller, E., Monadanaro, A., Di Febbraro, M., Lemmon, D., Castiglione, S., and Melchionna, M.: Climate shifts orchestrated hominin interbreeding events across Eurasia, Science, 381, 699–704, https://doi.org/10.1126/science.add4459, 2023.

Russon, T., Elliot, M., Sadekov, A., Cabioch, G., Corrège, T., and De Deckker, P.: Inter-hemispheric asymmetry in the early Pleistocene Pacific warm pool, Geophys. Res. Lett., 37, L11601, https://doi.org/10.1029/2010GL043191, 2010.

Schneider, T.: Feedback of Atmosphere-Ocean Coupling on Shifts of the Intertropical Convergence Zone, Geophys. Res. Lett., 44, 11644–11653, https://doi.org/10.1002/2017GL075817, 2017.

Schneider, T., Bischoff, T., and Haug, G. H.: Migrations and dynamics of the intertropical convergence zone, Nature, 513, 45–53, https://doi.org/10.1038/nature13636, 2014.

Schneider von Deimling, T., Ganopolski, A., Held, H., and Rahmstorf, S.: How cold was the Last Glacial Maximum?, Geophys. Res. Lett., 33, L14709, https://doi.org/10.1029/2006GL026484, 2006.

Screen, J. A., Bracegirdle, T. J., and Simmonds, I.: Polar Climate Change as Manifest in Atmospheric Circulation, Curr. Clim. Change Rep., 4, 383–395, https://doi.org/10.1007/s40641-018-0111-4, 2018.

Singarayer, J. S. and Valdes, P. J.: High-latitude climate sensitivity to ice-sheet forcing over the last 120 kyr, Quaternary Sci. Rev., 29, 43–55, https://doi.org/10.1016/j.quascirev.2009.10.011, 2010.

Smith, R. S. and Gregory, J.: The last glacial cycle: transient simulations with an AOGCM, Clim. Dynam., 38, 1545–1559, https://doi.org/10.1007/s00382-011-1283-y, 2012.

Stap, L. B., van de Wal, R. S. W., de Boer, B., Kohler, P., Hoencamp, J. H., Lohmann, G., Tuenter, E., and Lourens, L. J.: Modeled Influence of Land Ice and CO_2 on Polar Amplification and Paleoclimate Sensitivity During the Past 5 Million Years, Paleoceanogr. Paleoclim., 33, 381–394, https://doi.org/10.1002/2017pa003313, 2018.

Stein, K., Timmermann, A., Kwon, E. Y., and Friedrich, T.: Timing and magnitude of Southern Ocean sea ice/carbon cy-

cle feedbacks, P. Natl. Acad. Sci. USA, 117, 4498–4504, https://doi.org/10.1073/pnas.1908670117, 2020.

Stone, P. H.: Constraints on dynamical transports of energy on a spherical planet, Dynam. Atmos. Oceans, 2, 123–139, https://doi.org/10.1016/0377-0265(78)90006-4, 1978.

Stott, L., Timmermann, A., and Thunell, R.: Southern Hemisphere and Deep-Sea Warming Led Deglacial Atmospheric CO_2 Rise and Tropical Warming, Science, 318, 435–438, https://doi.org/10.1126/science.1143791, 2007.

3Ma-Data: Transient 3Ma model simulatation data, https://climatedata.ibs.re.kr. (last access: 11 October 2023), 2023.

Tiedemann, R., Sarnthein, M., and Shackleton, N. J.: Astronomic timescale for the Pliocene Atlantic $\delta^{18}O$ and dust flux records of Ocean Drilling Program Site 659, Paleoceanography, 9, 619–638, https://doi.org/10.1029/94PA00208, 1994.

Tierney, J. E., Zhu, J., King, J., Malevich, S. B., Hakim, G. J., and Poulsen, C. J.: Glacial cooling and climate sensitivity revisited, Nature, 584, 569–573, https://doi.org/10.1038/s41586-020-2617-x, 2020.

Tigchelaar, M. and Timmermann, A.: Mechanisms rectifying the annual mean response of tropical Atlantic rainfall to precessional forcing, Clim. Dynam., 47, 271–293, https://doi.org/10.1007/s00382-015-2835-3, 2016.

Tigchelaar, M., Timmermann, A., Pollard, D., Friedrich, T., and Heinemann, M.: Local insolation changes enhance Antarctic interglacials: Insights from an 800,000-year ice sheet simulation with transient climate forcing, Earth Planet. Sc. Lett., 495, 69–78, https://doi.org/10.1016/j.epsl.2018.05.004, 2018.

Tigchelaar, M., Timmermann, A., Friedrich, T., Heinemann, M., and Pollard, D.: Nonlinear response of the Antarctic Ice Sheet to late Quaternary sea level and climate forcing, The Cryosphere, 13, 2615–2631, https://doi.org/10.5194/tc-13-2615-2019, 2019.

Timm, O. and Timmermann, A.: Simulation of the last 21 000 years using accelerated transient boundary conditions, J. Climate, 20, 4377–4401, https://doi.org/10.1175/jcli4237.1, 2007.

Timm, O., Timmermann, A., Abe-Ouchi, A., Saito, F., and Segawa, T.: On the definition of seasons in paleoclimate simulations with orbital forcing, Paleoceanography, 23, PA2221, https://doi.org/10.1029/2007pa001461, 2008.

Timmermann, A. and Friedrich, T.: Late Pleistocene climate drivers of early human migration, Nature, 538, 92–95, https://doi.org/10.1038/nature19365, 2016.

Timmermann, A., Lorenz, S. J., An, S.-I., Clement, A., and Xie, S.-P.: The Effect of Orbital Forcing on the Mean Climate and Variability of the Tropical Pacific, J. Climate, 20, 4147–4159, https://doi.org/10.1175/jcli4240.1, 2007.

Timmermann, A., Timm, O., Stott, L., and Menviel, L.: The Roles of CO_2 and Orbital Forcing in Driving Southern Hemispheric Temperature Variations during the Last 21 000 Yr, J. Climate, 22, 1626–1640, https://doi.org/10.1175/2008JCLI2161.1, 2009.

Timmermann, A., Knies, J., Timm, O. E., Abe-Ouchi, A., and Friedrich, T.: Promotion of glacial ice sheet buildup 60–115 kyr B.P. by precessionally paced Northern Hemispheric meltwater pulses, Paleoceanography, 25, PA4208, https://doi.org/10.1029/2010pa001933, 2010.

Timmermann, A., Sachs, J., and Timm, O. E.: Assessing divergent SST behavior during the last 21 ka derived from alkenones and G. ruber-Mg/Ca in the equatorial Pacific, Paleoceanography, 29, 680–696, https://doi.org/10.1002/2013pa002598, 2014a.

Timmermann, A., Friedrich, T., Timm, O. E., Chikamoto, M. O., Abe-Ouchi, A., and Ganopolski, A.: Modeling Obliquity and CO_2 Effects on Southern Hemisphere Climate during the Past 408 ka, J. Climate, 27, 1863–1875, https://doi.org/10.1175/jcli-d-13-00311.1, 2014b.

Timmermann, A., Yun, K. S., Raia, P., Ruan, J. Y., Mondanaro, A., Zeller, E., Zollikofer, C., de Leon, M. P., Lemmon, D., Willeit, M., and Ganopolski, A.: Climate effects on archaic human habitats and species successions, Nature, 604, 495–501, https://doi.org/10.1038/s41586-022-04600-9, 2022.

Torrence, C. and Compo, G. P.: A Practical Guide to Wavelet Analysis, B. Am. Meteorol. Soc., 79, 61–78, https://doi.org/10.1175/1520-0477(1998)079<0061:Apgtwa>2.0.Co;2, 1998.

Varma, V., Prange, M., and Schulz, M.: Transient simulations of the present and the last interglacial climate using the Community Climate System Model version 3: effects of orbital acceleration, Geosci. Model Dev., 9, 3859–3873, https://doi.org/10.5194/gmd-9-3859-2016, 2016.

Willeit, M. and Ganopolski, A.: The importance of snow albedo for ice sheet evolution over the last glacial cycle, Clim. Past, 14, 697–707, https://doi.org/10.5194/cp-14-697-2018, 2018.

Willeit, M., Ganopolski, A., Calov, R., and Brovkin, V.: Mid-Pleistocene transition in glacial cycles explained by declining CO_2 and regolith removal, Sci. Adv., 5, eaav733, https://doi.org/10.1126/sciadv.aav7337, 2019.

Yamanouchi, T. and Charlock, T. P.: Effects of clouds, ice sheet, and sea ice on the Earth radiation budget in the Antarctic, J. Geophys. Res.-Atmos., 102, 6953–6970, https://doi.org/10.1029/96JD02866, 1997.

Yang, H., Li, Q., Wang, K., Sun, Y., and Sun, D.: Decomposing the meridional heat transport in the climate system, Clim. Dynam., 44, 2751–2768, https://doi.org/10.1007/s00382-014-2380-5, 2015.

Yarincik, K. M., Murray, R. W., and Peterson, L. C.: Climatically sensitive eolian and hemipelagic deposition in the Cariaco Basin, Venezuela, over the past 578,000 years: Results from Al/Ti and K/Al, Paleoceanography, 15, 210–228, https://doi.org/10.1029/1999PA900048, 2000.

Yin, Q., Berger, A., Driesschaert, E., Goosse, H., Loutre, M. F., and Crucifix, M.: The Eurasian ice sheet reinforces the East Asian summer monsoon during the interglacial 500 000 years ago, Clim. Past, 4, 79–90, https://doi.org/10.5194/cp-4-79-2008, 2008.

Yu, S. and Pritchard, M. S.: A Strong Role for the AMOC in Partitioning Global Energy Transport and Shifting ITCZ Position in Response to Latitudinally Discrete Solar Forcing in CESM1.2, J. Climate, 32, 2207–2226, https://doi.org/10.1175/jcli-d-18-0360.1, 2019.

Zeller, E., Timmermann, A., Yun, K. S., Raia, P., Stein, K., and Ruan, J. Y.: Human adaptation to diverse biomes over the past 3 million years, Science, 380, 604–608, https://doi.org/10.1126/science.abq1288, 2023.

Zhang, S., Yu, Z. F., Gong, X., Wang, Y., Chang, F. M., Lohmman, G., Qi, Y. Q., and Li, T. G.: Precession cycles of the El Nino/Southern oscillation-like system controlled by Pacific upper-ocean stratification, Commun. Earth Environ., 2, 239, https://doi.org/10.1038/s43247-021-00305-5, 2021.